Aalto University
School of Science
Master's Programme in Engineering Physics

Zhennan Kou

An empirical potential study of first-order Raman scattering in defective monolayer MoS_2

Master's Thesis
Espoo, March 22, 2019

Supervisor: Professor Martti Puska, Aalto University
Advisors: Dr. Hannu-Pekka Komsa
M.Sc. Arsalan Hashemi

Aalto University
School of Science
Master's Programme in Engineering Physics

ABSTRACT OF
MASTER'S THESIS

Author: Zhennan Kou

Title:
An empirical potential study of first-order Raman scattering in defective monolayer MoS_2

Date:	March 22, 2019	**Pages:**	66
Major:	Physics of Advanced Materials	**Code:**	SCI3057
Supervisor:	Professor Martti Puska		
Advisors:	Dr. Hannu-Pekka Komsa M.Sc. Arsalan Hashemi		

Semiconducting monolayer molybdenum disulfide (1H phase monolayer MoS_2), a famous member of two-dimensional inorganic materials, is well known by its direct bandgap. With the bandgap, it makes unique opportunities possible for (opto-)electronic applications and heat transport applications. Defects, the inevitable members of solid materials, can play an important role in tailoring various properties.

Raman spectroscopy is known as an essential and versatile tool for searching crystallinity, quality of materials under defects, and strain condition. We studied Raman spectra for various types of defective monolayer MoS_2 containing vacancies and antisites. We monitored the effect of each type of defect on prominent modes as a function of the defect density. We showed that the in-plane Raman mode is quite sensitive to defects. Also, for some cases, the out-of-plane mode can be used as a defect indicator. Phonons at the edge of the Brillouin zone can make low-frequency Raman active modes. Moreover, we found that for some vacancies, there are characteristic peaks, which arise mainly because of the influence of vacancies on localized strain and symmetry breaking. We found that the localized strain effect is one of the most critical effects causing the primary Raman peak shifts of the defective MoS_2. To explain the Raman peak shifts, we built two simple models, and through calculations, we showed that our models work well in predicting the Raman peak shift tendencies. Furthermore, through our models, we quickly got the conclusion that the mass effect and the disappearance of bonds caused by defects are the main reasons for the system's Raman peak shifts.

In this thesis, the primary methods used in the simulation are Phonopy calculations combined with empirical potentials (EP), and making projections between each observed mode and the two Raman active modes of primitive monolayer MoS_2. We showed that our method is economic and accurate enough when compared with first principles calculations. Our method presents a quick way to simulate Raman spectroscopy.

Keywords: Raman shift, monolayer MoS_2, defect, vibrational mode, empirical potential, strain effect, mass effect, characteristic peak

Language: English

Acknowledgements

I'm grateful to Prof. Martti Puska, Dr. Hannu-Pekka Komsa, and M.Sc. Arsalan Hashemi for their extraordinary support and insightful feedback on this thesis. I would also like to thank Dr. Arkady Krasheninnikov and Dr. Zheyong Fan for discussions.

Espoo, March 22, 2019

Zhennan Kou

Abbreviations and Acronyms

EP	Empirical potential
REBO	Reactive empirical bond order
LJ	Lennard-Jones
DFT	Density functional theory
DOS	Density of states
GDOS	Γ weighted density of states
RGDOS	Raman weighted GDOS
BZ	Brillouin zone
FBZ	First Brillouin zone
PC	Primitive cell
SC	Supercell
vdW	Van der Waals

Contents

Chapter 1

Introduction

Since the discovery of graphene in 2004, an enormous amount of attention has been paid on two-dimensional (2D) materials such as transition metal dichalcogenides (TMDs) for their unique electronic, optical, and mechanical properties [1–5]. In particular, the prototypical MoS_2 is a famous member of TMDCs library in its monolayer structure due to the direct optical band gap which has created new opportunities for (opto) electronic devices [6].

Defects, produced unintentionally during fabrication and measurements [7, 8] or intentionally using electron and ion beam irradiation [9], are an inseparable part of crystal structures. In cases where the performance of devices strongly depends on the quality of the sample, the introduction of defects deteriorates noble features. Different types of defects can also be used to create new functionalities and improve material properties. Examples include managing the electronic properties and the thermal properties [10, 11]. Therefore, it is always important to understand the types, concentration and even arrangement of defects in structures.

First-order nonresonant Raman spectroscopy is a non-destructive tool that makes it possible to understand the sample quality and even defect quantity. Experimentally, this technique is based on the measurements of scattered light intensity and frequency. Theoretically, one can calculate Raman spectra from density functional theory (DFT), where the change of medium polarizability resulted by vibrational modes is studied. Of course, this approach is computationally too heavy for defect calculations with large supercells (SCs). Then, it is essential to develop a new Raman spectra simulation method to study practical problems.

In this study, we first introduce recent researches into MoS_2 and the motivation of research. Then, the theoretical background is discussed in chapter 2. Chapter 3 contains the symmetry point group information and provides our model to study lattice vibrations. The detailed analyses of results, including the phonon dispersion curve, the simulated Raman spectra, and the role of defects in the shape of the Raman spectra can be found in chapter 4. Finally, we conclude in chapter 5.

1.1 Motivation

As mentioned above, Raman spectroscopy provides a wealth of information about sample quality. Although the Raman spectra of pristine monolayer MoS_2 has been intensely

investigated, there are still problems/questions for defective monolayer MoS_2 to answer about. For example, how to understand (i) the shifts of prominent Raman-active modes, in-plane E_g at 390 cm^{-1} and out-of-plane A_g^1 at 409 cm^{-1}, observed [12] in bulk MoS_2, (ii) the changes in broadening and isotropic shape of peaks, (iii) the advents of new peaks appeared due to the absence of momentum conservation. Specifically, it is desirable to find out which type of defect at which concentration and arrangement are able to shape Raman spectra.

The understanding of such a correlation between defect concentration, arrangement, and type in a Raman spectrum is highly demanding by DFT. Few computational studies have been carried out [13, 14]. A common problem in all of these is the high concentration of defects, necessitated by the fairly small size of the SC that also limits the randomness. For the number of atoms N (and minimum accessible defect concentration N^{-1}), the number of displacements is $3N$, and the semilocal DFT calculations generally scale as N^3, thereby yielding the total computational cost scaling as N^4. In 2D materials, the scaling with respect to the SC size $m \times m$ is then m^8.

Making use of the recent improvement in computational Raman spectroscopy proposed by Hashemi *et al.* [15], who applied mass-approximation and projection operators to make Raman spectroscopy possible for the study of alloys and impurities, we evaluate Raman spectroscopy for large scale defective monolayer MoS_2 using empirical potential (EP) as the restoring force calculator. Owing to the reliable empirical potential, the speed of computational time and amount of required resources decreases significantly. Thus it also lets us to directly consider the effects of all various types of vacancies and anti-sites that gives a good opportunity to have a more realistic view on the effects of defects.

By using EP for calculations, we get the chance to further study the origin of the shifts of prominent Raman-active modes, as well as the formation of new peaks by defects. By carefully analyzing and testing all the possible influencing factors behind the phenomenons mentioned above, this work will provide us a better understanding of the role of defects for the lattice structure and vibrational modes. Once our results show the effect of one kind of defects on shifting the Raman modes or formation of new peaks in specific frequencies, they will help in experiments by providing fingerprints to detect and identify defects.

Chapter 2

Theoretical Background

In this chapter, we go through the theoretical concepts of phonon and Raman scattering. Then, we introduce the concepts of the phonon density of states (DOS), Γ-weighted density of states (GDOS), and Raman-active Γ-weighted density of states (RGDOS).

2.1 Phonons

Vibrational properties of solids are central for a large number of physical phenomena, including phase stability and thermal conduction. In crystalline solids, the vibrational motion of atoms is periodic and commonly described using vibrational modes (phonons)− quasi-particles that represent collective excitations of the lattice. It is well known that phonons obey the Bose−Einstein statistics [16]. In thermal equilibrium, the average number of phonons with frequency ω_i is

$$n(\omega_i) = \frac{1}{e^{\hbar\omega_i/k_BT} - 1}. \tag{2.1}$$

It is noteworthy that the phonon behavior of a kind of material mostly depends on the symmetry of its structure. Following from the lattice translational periodicity, $f(\mathbf{r}+\mathbf{T}) = f(\mathbf{r})$, the problem of the dynamics of the atoms is reduced to that in a primitive unit cell. To simplify the problem of atomic vibrations, we make two approximations:

(i) **Adiabatic approximation**

It is convenient to visualize an atom in a solid in terms of ion cores and valence electrons. As ion cores are much heavier than electrons, their motion can be treated separately. As a consequence of this approximation, the motion of ion cores is determined in a potential field generated by the average motion of electrons. While dealing with the motion of electrons, it is assumed that ion positions are fixed.

(ii) **Harmonic approximation**

The potential energy of a solid can be represented by the Taylor expansion of the potential energy surface in tiny ionic displacements $\mathbf{u} = \mathbf{R}-\mathbf{R}_0$ away from the equilibrium positions $\mathbf{R}_0$, as shown in fig.2.1,

$$V = V_0 + \Phi_i^\alpha u_i^\alpha + \frac{1}{2}\Phi_{ij}^{\alpha\beta} u_i^\alpha u_j^\beta + \frac{1}{3}\Phi_{ijk}^{\alpha\beta\gamma} u_i^\alpha u_j^\beta u_k^\gamma + \cdots, \tag{2.2}$$

where $\Phi_i^\alpha = \frac{\partial V}{\partial u_i^\alpha}, \Phi_{ij}^{\alpha\beta} = \frac{\partial^2 V}{\partial u_i^\alpha \partial u_j^\beta}, \cdots$ are the force constants corresponding to the increasing orders of the expansion. Latin indices i indicate atomic labels, while Greek indices α run

over the Cartesian coordinates x, y, z. V_0 is a constant term (reference potential) which is commonly ignored when dealing with lattice dynamics. The first-order force constant is also dropped since the expansion in displacement is made around an equilibrium lattice configuration with vanishing forces. Truncating the potential after the second-term results in the harmonic approximation. In this classical picture, an atom in the crystal vibrates as a three-dimensional (3D) simple harmonic oscillator joined by harmonic springs to its neighbors. In the harmonic approximation, we have non-interacting phonons with an infinite lifetime.

To describe the lattice dynamics problem in the harmonic approximation, which results in the relationship between the energy of a phonon and its wave vector, we first consider a linear chain of atoms and then extend the idea to a general form of 3D lattices.

2.1.1 Diatomic linear chain

First, let us introduce the basic phonon properties by using a simple model [17], a one-dimensional crystal with two different types of atoms A and B which constitute the unit cell. For all the atoms to have an identical environment, let us assume a closed chain so that the $(N+1)th$ atom is the $1st$ atom, *i.e.*, a condition for periodicity. We also suppose that the equilibrium distance between two neighboring atoms (lattice vector) is a and only nearest-neighbor forces are significant. Once there is vibration, every atom will gain a small shift u. For instance, the $2nth$ atom shifts by u_{2n}. The details are shown in fig.2.1. Following Newton's second law and Hooke's law, the equation of motion of the $2nth$ and

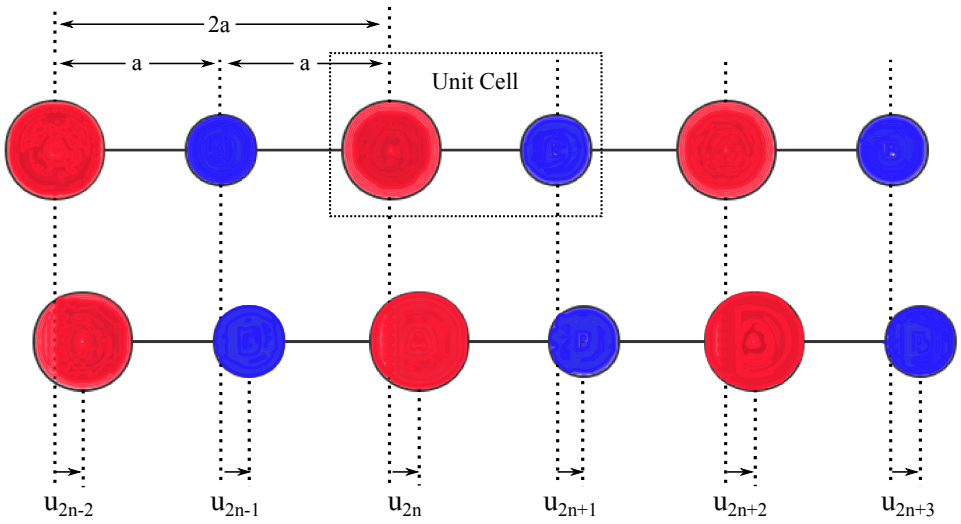

Figure 2.1: Diatomic linear chain with alternating masses m (blue balls) and M (red balls). The upper row is in equilibrium and the lower row is a snapshot of a vibrating chain.

$(2n+1)th$ atoms, with masses M and m, respectively, can easily be written as

$$\begin{cases} M\frac{d^2u_{2n}}{dt} = K\left(u_{2n+1} + u_{2n-1} - 2u_{2n}\right) \\ m\frac{d^2u_{2n+1}}{dt} = K\left(u_{2n} + u_{2n+2} - 2u_{2n+1}\right) \end{cases}, \tag{2.3}$$

where K is the nearest-neighbor force constant. For a periodic potential, the normal modes of vibrations are expressed as travelling waves obeying the Bloch theorem:

$$\begin{cases} u_{2n} = Ae^{i(\omega t - 2naq)} \\ u_{2n+1} = Be^{i(\omega t - (2n+1)aq)} \end{cases}, \tag{2.4}$$

where q is the wave vector, ω is the angular frequency of the wave, A and B are the amplitudes of motions of the $2nth$ and $(2n+1)th$ atoms, respectively. Inserting eq.2.4 in eq.2.3, solutions can be found by solving

$$\begin{cases} (M\omega^2 - 2\beta)\, A + 2\beta\cos(aq)B = 0 \\ 2\beta\cos(aq)A + (m\omega^2 - 2\beta)\, B = 0 \end{cases}. \tag{2.5}$$

If there are solutions for eq.2.5, it's secular equation should be zero:

$$|D_{ij} - \omega^2\delta_{ij}| = \begin{vmatrix} M\omega^2 - 2\beta & 2\beta\cos(aq) \\ 2\beta\cos(aq) & m\omega^2 - 2\beta \end{vmatrix} = 0. \tag{2.6}$$

Note that D is called as the dynamical matrix, which is deeply introduced later on. This 1D chain has only $1 \times 2 = 2$ phonon modes since each atom has only one degree of freedom. This corresponds to the size of matrix (2×2), too. One can solve eq.2.6 between the wave vector and the frequency,

$$\omega_{\pm}^2 = \beta\left(\frac{1}{M} + \frac{1}{m}\right) \pm \beta\sqrt{\left(\frac{1}{M} + \frac{1}{m}\right)^2 - \frac{4\sin^2 aq}{Mm}}. \tag{2.7}$$

Here, the "+" part of eq.2.7 is the optical branch, and the "−" part is the acoustic branch. The phonon dispersion curves that show the relation between the frequency of normal vibrational modes and wave vectors along high-symmetry directions are shown in fig.2.2. It is worth to note that (i) the dispersion curve shows the translational symmetry in q space: $\omega(q + G_n) = \omega(q)$, where G_n is the magnitude of a reciprocal lattice vector corresponding to the chain, and (ii) $\omega(q)$ is a symmetric function between q and $-q$. Each q value represents a phonon with energy $\hbar\omega(q)$.

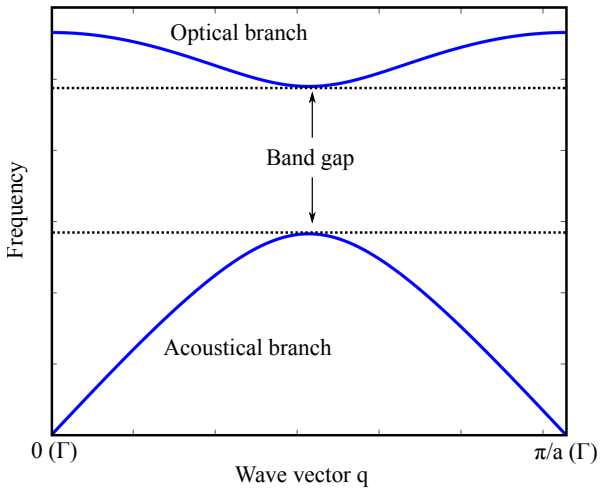

Figure 2.2: Phonon dispersion curves of a 1D chain with two different types of atoms.

2.1.2 General form of phonon dispersion relations

The main part of the derivation in this section is from reference [17].

Consider a crystal with N atoms per unit cell, and let $\mathbf{u}(lb)$ represent the displacement vector of the bth atom in the lth unit cell. Eq.2.2 can be rewritten as

$$V = V_0 + \sum_{lb\alpha} \frac{\partial V}{\partial u_\alpha(lb)}|_0 u_\alpha(lb) + \frac{1}{2}\sum_{lbl'b'}\sum_{\alpha\beta} \frac{\partial^2 V}{\partial u_\alpha(lb)\partial u_\beta(l'b')}|_0 u_\alpha(lb)u_\beta(l'b') + \cdots$$

As mentioned above, in the harmonic approximation we have

$$V = \frac{1}{2}\sum_{lbl'b'}\sum_{\alpha\beta} \frac{\partial^2 V}{\partial u_\alpha(lb)\partial u_\beta(l'b')}|_0 u_\alpha(lb)u_\beta(l'b').$$

Then the equation of motion becomes a generalisation of eq.2.3

$$m_b\ddot{u}_\alpha(lb) = -\sum_{l'b'\beta} \Phi_{\alpha\beta}(lb;l'b')u_\beta(l'b'), \tag{2.8}$$

where $\Phi_{\alpha\beta}(lb;l'b') = \frac{\partial^2 V}{\partial u_\alpha(lb)\partial u_\beta(l'b')}|_0$ denotes the interatomic force constant matrix, m_b is the mass of the bth atom, and $\alpha = x, y, z$. In fact $\Phi_{\alpha\beta}(lb;l'b')u_\beta(l'b')$ represents the negative of the linear force on the atom (lb) along the α direction due to a unit of displacement of the atom $(l'b')$ along the β direction and it obeys two important symmetry relations.

From the *lattice translational symmetry* we have

$$\Phi_{\alpha\beta}(lb;l'b') = \Phi_{\alpha\beta}(0b;(l'-l)b'),$$

and the *infinitesimal translation invariance* of the crystal leads to

$$\Phi_{\alpha\beta}(lb;lb) = -\sum_{l'b'\neq lb} \Phi_{\alpha\beta}(lb;l'b').$$

The latter equation means when all atoms are equally displaced, there is no force on any atom. Using the lattice translational symmetry, eq.2.8 can be expressed as

$$m_b\ddot{u}_\alpha(lb) = -\sum_{l'b'\beta} \Phi_{\alpha\beta}(0b;l'b')u_\beta(l'b'). \tag{2.9}$$

To solve eq.2.9, we try a solution of the form

$$u_\alpha = \frac{1}{\sqrt{m_b}}\sum_{\mathbf{q}} U_\alpha(\mathbf{q};b)e^{\mathrm{i}(\mathbf{q}\cdot\mathbf{x}(l)-\omega t)},$$

where $\mathbf{x}(l)$ is the equilibrium position vector of the lth unit cell and $U_\alpha(\mathbf{q};b)$ is independent of l. By substituting this into eq.2.9 we get

$$\omega^2 U_\alpha(\mathbf{q};b) = \sum_{b'\beta} D_{\alpha\beta}(bb';\mathbf{q})U_\beta(\mathbf{q};b'), \tag{2.10}$$

where $D_{\alpha\beta}(bb';\mathbf{q})$ is the dynamical matrix and is expressed as [18]

$$D_{\alpha\beta}(bb';\mathbf{q}) = \frac{1}{\sqrt{m_b m_{b'}}} \sum_{l'} \Phi_{\alpha\beta}(0b; l'b') e^{\mathrm{i}(\mathbf{q}\cdot\mathbf{x}(l))}.$$

Since D is Hermitian, eq.2.10 produces $3N$ real eigenvalues $\omega^2(\mathbf{q}, s)$, where $s = 1, 2, 3, \cdots, 3N$. We consider $\omega(\mathbf{q}, s)$ as real to meet the stability of the crystal. From the time reversal symmetry it follows

$$\omega^2(\mathbf{q}, s) = \omega^2(-\mathbf{q}, s),$$

and hence

$$\omega(\mathbf{q}, s) = \omega(-\mathbf{q}, s),$$

which meets the observation (ii) of section 2.1.1.

For each of the $3N$ eigenvalues $\omega^2(\mathbf{q}, s)$ corresponding to a given $\mathbf{q}$ there exist an eigenvector $\mathbf{e}(b;\mathbf{q}, s)$, which is the normalized U term in eq.2.10. Thus eq.2.10 can be written as

$$\omega^2(\mathbf{q}, s) e_\alpha(b;\mathbf{q}, s) = \sum_{b'\beta} D_{\alpha\beta}(bb';\mathbf{q}) e_\beta(b';\mathbf{q}, s). \tag{2.11}$$

The components of $\mathbf{e}(b;\mathbf{q}, s)$ satisfy the following orthogonality and completeness relations:

$$\sum_{b\alpha} e^*_\alpha(b;\mathbf{q}, s) e_\alpha(b;\mathbf{q}, s') = \delta_{ss'},$$

$$\sum_{s} e^*_\beta(b';\mathbf{q}, s) e_\alpha(b;\mathbf{q}, s) = \delta_{bb'}\delta_{\alpha\beta}.$$

The complete solutions to the eigenproblem in eq.2.11 are sought in terms of $\omega = \omega(\mathbf{q}, s)$ (called the phonon dispersion relation for eigenvalues) and $\mathbf{e} = \mathbf{e}_s(\mathbf{q})$ (the dispersion relation for eigenvectors). The index s corresponds to the *sth* branch in the order of the increasing frequency and it changes in the range of degree of freedoms, as mentioned before. For 3D cases, there will be three *acoustic* branches such that $\omega(\mathbf{q}) \to 0$ as $\mathbf{q} \to 0$ and $3N - 3$ optical branches, where N is the total number of atoms, such that $\omega(\mathbf{q}) \to$ constant as $\mathbf{q} \to 0$. Atomic vibrations corresponding to any of the branches can be either constant as *longitudinal* (atoms vibrate along the wave propagation direction), *i.e.*, $\mathbf{e} \parallel \mathbf{q}$ or *transverse* (atoms vibrate perpendicular the direction of wave propagation), *i.e.*, $\mathbf{e} \perp \mathbf{q}$ or a mixture of both. Later, we will discuss the information that can be extracted from phonon dispersion curves in depth.

2.1.3 Phonon density of states

One of the most important quantities related to the study of lattice dynamics is the phonon density of states (DOS). It is defined as the number of phonon states between the frequencies ω and $\omega + \mathrm{d}\omega$, or equivalently, between the wave vectors $\mathbf{q}$ and $\mathbf{q} + \mathrm{d}\mathbf{q}$. Assume that the dispersion relation in a crystal is known, then a general expression for DOS can be obtained by using the periodic boundary conditions:

$$\mathbf{u}(\mathbf{r}) \equiv \mathbf{u}(\mathbf{r} + l a_x \hat{\mathbf{x}}),$$

$$\mathbf{u}(\mathbf{r}) \equiv \mathbf{u}(\mathbf{r} + ma_y\hat{\mathbf{y}}),$$
$$\mathbf{u}(\mathbf{r}) \equiv \mathbf{u}(\mathbf{r} + na_z\hat{\mathbf{z}}),$$

where (l, m, n) are integers and (a_x, a_y, a_z) are the primitive unit cell lattice constants in $(\hat{\mathbf{x}}, \hat{\mathbf{y}}, \hat{\mathbf{z}})$ directions, respectively. Thus, (la_x, ma_y, na_z) represents the size of SC. Inspired by the solution mentioned in section 2.1.2, for example in $\hat{\mathbf{x}}$ direction, one can obtain

$$e^{\mathrm{i}(q_x x + q_y y + q_z z)} = e^{\mathrm{i}(q_x(x+la_x) + q_y y + q_z z)}.$$

Thus $q_x = \frac{2\pi n}{la_x}$, where $n = 0, \pm1, \pm2, \cdots$, are the allowed $\mathbf{q}_x$ values with one $\mathbf{q}$ confined to a length of $\frac{2\pi}{la_x}$. Similarly, using also the conditions for the $\hat{\mathbf{y}}$ and $\hat{\mathbf{z}}$ directions result in a volume $\Omega = \frac{8\pi^3}{la_x ma_y na_z} = \frac{8\pi^3}{V}$ that confines one $\mathbf{q}$ point.

Clearly, to derive an expression for DOS we need to find the number of $\mathbf{q}$-values, $g(\mathbf{q})$, in the range $\mathrm{d}\mathbf{q}$ or correspondingly the number of frequencies, $g(\omega)$, in the frequency interval $\mathrm{d}\omega$. Consider two surfaces of constant frequencies ω and $\omega + \mathrm{d}\omega$. Assume an elementary area $\mathrm{d}S_\omega$ on the surface ω that makes the element of the cylinder that connects the surfaces. The volume of this cylinder with height $\mathrm{d}q$ is

$$\int \mathrm{d}S_\omega \mathrm{d}q = \int \mathrm{d}S_\omega \frac{\mathrm{d}\omega}{|\bigtriangledown_q \omega|}, \tag{2.12}$$

where we have used the fact that $\bigtriangledown_q \omega$ is perpendicular to the constant ω surface.

Since a unit volume in the $\mathbf{q}$-space per $\mathbf{q}$ value is $\frac{1}{\Omega} = \frac{V}{8\pi^3}$, where V is the volume of solid, then the number of $\mathbf{q}$-values in the cylinder volume is

$$g(\omega) = \frac{V}{8\pi^3} \times \text{volume of cylinder} \equiv \frac{V}{8\pi^3} \int \mathrm{d}S_\omega \frac{\mathrm{d}\omega}{|\bigtriangledown_q \omega|}.$$

In numerical calculation, since the the number of mesh points is finite, one can use the follow equation

$$g(\omega) = constant \times \sum_{\mathbf{q_v}, s}^{FBZ} \Theta(\omega - \omega(\mathbf{q_v}, s)), \tag{2.13}$$

where FBZ is the abbreviation of the first Brillouin zone, and

$$\Theta = \begin{cases} 1, & \text{for } |\omega - \omega(\mathbf{q_v}, s)| \leq \frac{\Delta\omega}{2} \\ 0, & \text{otherwise} \end{cases}. \tag{2.14}$$

2.2 Raman effect

The general explanation of the Raman effect is known as the interaction of the incident light of energy $\hbar\omega_\mathrm{i}$ with the crystal to create or destroy one or more phonons and the energy $\hbar\omega$ gained or lost by the lattice is compensated by a decrease or increase in the scattered light energy $\hbar\omega_\mathrm{s}$ ($\omega_\mathrm{s} = \omega_\mathrm{i} \pm \omega$). The part of the scattered light of lower frequency than the incident light is called the Stokes component, while the part of the scattered light of higher frequency is called anti-Stokes component. When the temperature of the medium is zero (T = 0 K), no lattice vibrations exist and we assume that only the Stokes part of

the scattering is activated. Two noteworthy points about Raman spectroscopy are (i) for a first-order Raman scattering, one considers only one phonon involved in the scattering processes, and (ii) when the energy of the applied incident light becomes less than the optical band gap of the medium (material), one can ignore electrons in the scattering processes.

As mentioned in section 2.1.2, the phonon wave vector can take on any value lying in the FBZ, the maximum value being of the order of $\frac{\pi}{a}$, where a is the lattice constant. For example, for monolayer MoS_2 it is typically of the order of $1 \times 10^8 \text{cm}^{-1}$. Incident light with a wave number of $2 \times 10^4 \text{cm}^{-1}$ (vacuum) has a wave vector inside the crystal of order $3 \times 10^4 \text{cm}^{-1}$ (in-material) (wave vector = refractive index $\times$ wave number in vacuum) and for scattering of light through 90°, wave vector conservation requires the wave vector of phonon created to be $\sim \sqrt{2} \times 3 \times 10^4 \text{cm}^{-1}$. This is small compared to $\frac{\pi}{a}$. In other words, the important phonons in the first-order Raman effect have wavelengths very long compared to the lattice constant, *i.e.*, they are close to the Γ-point (center of the FBZ). This leads to a great simplification in the discussion of their properties.

Let us consider all phonons at the center of FBZ of a pristine crystal. Among optical phonons, which are excited and can be candidates of scattering, those modifying the response of crystal to the electromagnetic field of incident light are called as Raman-active modes. To simplify, in the macroscopic point of view, consider a medium or crystal with electric susceptibility χ that should be a second rank tensor in general. The incident electromagnetic field is defined as

$$\mathbf{E}_\text{i}(\mathbf{r}, t) = \mathbf{E}_\text{i}(\mathbf{k}_\text{i}, \omega_\text{i}) \cos(\mathbf{k}_\text{i} \cdot \mathbf{r} - \omega_i t),$$

leading to polarization

$$\mathbf{P}(\mathbf{r}, t) = \mathbf{P}_\text{i}(\mathbf{k}_\text{i}, \omega_\text{i}) \cos(\mathbf{k}_\text{i} \cdot \mathbf{r} - \omega_i t) = \chi(\mathbf{k}_\text{i}, \omega_\text{i}) \mathbf{E}_\text{i}(\mathbf{k}_\text{i}, \omega_\text{i}) \cos(\mathbf{k}_\text{i} \cdot \mathbf{r} - \omega_i t).$$

In the lattice, we have a set of phonons, each with an atomic displacement vector $\mathbf{u}(\mathbf{r}, t)$, that can be described as

$$\mathbf{u}(\mathbf{r}, t) = \sum_{\mathbf{k}_i} \mathbf{u}(\mathbf{k}_i, \omega_i) \cos(\mathbf{k}_i \cdot \mathbf{r} - \omega_i t).$$

Now, we can expand $\chi(\mathbf{k}_\text{i}, \omega_\text{i})$ in $\mathbf{u}(\mathbf{k}_i, \omega_i)$

$$\chi(\mathbf{k}_\text{i}, \omega_\text{i}) = \chi_0(\mathbf{k}_\text{i}, \omega_\text{i}) + \frac{\partial \chi}{\partial \mathbf{u}} \mathbf{u}(\mathbf{k}_i, \omega_i) + \cdots$$

and in the first-order level of approximation obtain the change in polarization induced by the phonon:

$$\mathbf{P}_\text{ind}(\mathbf{k}_i, \omega_i, \mathbf{u}) = \frac{\partial \chi}{\partial \mathbf{u}} \mathbf{u}(\mathbf{k}_i, \omega_i) \mathbf{E}_\text{i}(\mathbf{k}_\text{i}, \omega_\text{i}). \tag{2.15}$$

For the Γ-point and by replacing the component $\mathbf{u}(\mathbf{k}_i, \omega_i)$ with the component $\mathbf{e}(b; 0, s)$ which was mentioned in eq.2.11, eq.2.15 can be written as

$$\mathbf{P}_\text{ind}(\mathbf{e}) = \frac{1}{2} \frac{\partial \chi}{\partial \mathbf{e}(b; 0, s)} \mathbf{e}(b; 0, s) \mathbf{E}_\text{i}. \tag{2.16}$$

Finally, the intensity is proportional to [19]

$$I_s \sim \mid \mathbf{e}_i \cdot \frac{\partial \chi}{\partial \mathbf{e}(b;0,s)} \mathbf{e}(b;0,s) \cdot \mathbf{e}_s \mid^2, \tag{2.17}$$

where $\frac{\partial \chi}{\partial \mathbf{e}(b;0,s)} \mathbf{e}(b;0,s)$ gives the elements of the Raman tensor, R, that is shaped by following the symmetry of crystal. It is worth mentioning that the same approach can be applied for defective structures.

2.3 First Brillouin zone unfolding

To study realistic and sensible levels of impurity concentrations and arrangements, we exploit the SC approach to model different structures. The primitive cell (PC) is multiplied, *e.g.* by $M_x \times M_y \times M_z$ in different directions, as large as required and possible to calculate. Following the relation $\exp^{i\mathbf{G}.\mathbf{T}} = 1$, that maps a real space into the corresponding reciprocal space, the SC FBZ comes out smaller in a scale of $\frac{1}{M_x} \times \frac{1}{M_y} \times \frac{1}{M_z}$. In addition, the number of phonons becomes to $3n \times M_x \times M_y \times M_z$, where n denotes number of atoms in PC. This is illustrated in fig.2.3 for monolayer MoS_2 with $M_x = M_y = N$. As a

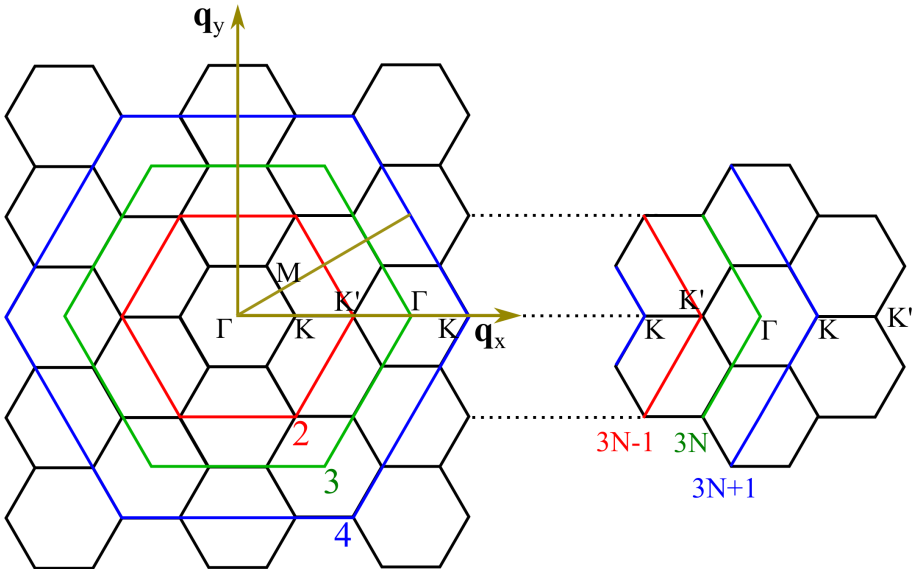

Figure 2.3: FBZ of monolayer MoS_2, extracted from [20]. The black lines represent the FBZ of SC. The red, green and blue lines are the Brillouin zones (BZ) of PC corresponding to SCs of $(3N-1) \times (3N-1)$, $3N \times 3N$ and $(3N+1) \times (3N+1)$, respectively.

result of folding, the phonon dispersions get complicated and extremely hard to discuss. To be directly compared with either experiment (*e.g.*, inelastic neutron scattering) or pristine system, one needs to unfold SC BZ into the FBZ of PC. The main advantage of this method is the ability to handle systems with the breaking of spatial translational symmetry. In order to unfold phonon dispersion curves, two steps need to be taken as follows:

(i) Finding the corresponding $\mathbf{q}$ in the PC BZ to each $\mathbf{Q}$ of the SC BZ

Let us use $\mathbf{r}_b$ and $\mathbf{R}_{lb}$ to represent the atom position vectors in PC and SC, respectively, where $b = 1, 2, \cdots, n$ and $l = 1, 2, \cdots M_x \times M_y \times M_z$. The vectors obey the relation $\mathbf{R}_{lb} = \mathbf{r}_b + \mathbf{T}_l$. Vectors $\mathbf{T}_l$ are the PC lattice point vectors. In the reciprocal space, the phonon wave vectors for PC and SC are denoted by $\mathbf{q}$ and $\mathbf{Q}$, respectively. They obey a similar relation

$$\mathbf{q} = \mathbf{Q} + \mathbf{G}_l.$$

The vector $\mathbf{G}_l$ is the reciprocal lattice point for SC.

(ii) Projection of the SC eigenfunctions on the PC counterparts

Now, suppose there are J vibrational modes in SC and I in PC. At the $\mathbf{Q}$ point in SC BZ (corresponding to the $\mathbf{q}$ point in PC BZ), we want to find the unfolded ith mode (i= 1,2,$\cdots$,I) of PC among all the SC modes. The way is to project all modes between SC and PC. Because of the orthonormality of the eigenfunctions, it is easy to find that the projection weight is a value between 0 and 1. If the SC is pristine, there will be one mode of SC in the $\mathbf{Q}$ point for which the eigenvector is the same as the one of the PC mode in the $\mathbf{q}$ point. It means that the projection weight between these two modes' eigenfunctions is 1. It is natural to define the projection weight as follow:

$$w^2_{ij,\mathbf{Q}}(\mathbf{q}) = | < \mathbf{e}^{PC,i} | \mathbf{e}^{SC,j} > |^2 = | \sum_{l,b} \mathbf{e}^{PC}(0b; \mathbf{q}i) \mathbf{e}^{SC}(lb; \mathbf{Q}j) |^2. \tag{2.18}$$

Where j=1,2,$\cdots$,J, and the summation is over all the atoms. Note that in this method, the knowledge of eigenfunctions in PC is needed. Besides this unfolding method, there is another unfolding method, where the basic idea is to do the projections on the plane waves [21].

2.4 RGDOS

In section 2.2 we mentioned that simulation of Raman spectra requires an enormous amount of resources, especially when the cell size is large. In this thesis, we mainly want to simulate large SCs with randomly distributed defects. Therefore it is nearly impossible to evaluate all the terms required in eq.2.17. Thus we need a cheaper way to calculate Raman spectra. In reference [22], Baroni *et al.* found that the GDOS (Γ-point weighted density of states) of PC can be used to approximate Raman spectra closely. However, this method requires that the frequencies of Raman-active modes and Raman-inactive modes are clearly separated. Here, we introduce the RGDOS (Raman intensity-weighted GDOS) [15] approximation.

The RGDOS calculation is based on the projection of SC modes to the Raman-active PC modes at the Γ point. The expression of the projection weight is eq.2.18, where $\mathbf{e}^{PC}$ only represents Raman-active eigenfunctions of PC, in which $\mathbf{q} = 0$.

When the symmetry of the defective SC does not heavily break, the modes in the SC with the same symmetry of Raman-active modes as in PC can be considered as Raman-active modes. Since the first-order Raman-active modes are only at the Γ point, the Raman-active modes of SC are folded to Raman-active modes of PC at the Γ point. Then RGDOS projection selects the Raman-active modes by the projection. Note that since the break of symmetry and the folding effect, some vibrational modes which were not

Raman-active before will be no more orthogonal to the Raman-active modes at the Γ point, and have then contributions to the Raman spectrum.

Thus, the RGDOS can represent the first-order Raman spectrum. The Raman tensor of a SC mode can be obtained by multiplying the Raman tensors of the PC modes with their projection weights. *i.e.*,

$$R^{SC,j} = \sum_i w_{ij} R^{PC,i}, \tag{2.19}$$

Note that the sum only goes over all PC Raman-active modes. Thus with eq.2.17, the Raman intensity is

$$I^{SC,j} \sim \sum_i w_{ij}^2 I^{PC,i}. \tag{2.20}$$

Note that in the above equation we assume that the cross terms $\sum_{i\neq k}(\mathbf{e}_s \cdot w_{ij} R^{PC,i} \cdot \mathbf{e}_i)^*(\mathbf{e}_s \cdot w_{kj} R^{PC,k} \cdot \mathbf{e}_i)$ are small and can be neglected. Eq.2.19 and eq.2.20 show that the RGDOS can represent the first-order Raman spectrum. In this thesis, what we are interested in is actually the frequencies of the Raman peaks, and in the RGDOS method, the frequencies for all the vibrational modes are known. Thus one can find the frequencies of simulated Raman peaks easily.

Chapter 3

Computational details and models

In this chapter, we first list various monolayer MoS_2 structures and their possible defects. Then, we introduce the empirical potential (EP) used in classical molecular dynamics (MD) calculations. To crosscheck results, we exploit the DFT framework discussed at the end of this chapter.

3.1 Structural properties

Monolayer molybdenum disulfide (1L-MoS_2) is a 2D crystal, consisting of three hexagonal atomic sheets. Each Mo plane is sandwiched by two S planes, and the atoms are bonded covalently. In the bulk structure, monolayers interact by weak van der Waals (vdW) forces that allow the exfoliation of bulk down to 1L-MoS_2. Structurally, the pristine 1L-MoS_2 has three stable phases with different electronic properties that are introduced as follows.

Octahedral phase

The octahedral phase MoS_2 has a trigonal symmetry and corresponds to the octahedral coordination of metal atoms and conventionally one refers to it as the 1T phase. The d^2sp^3 hybridization of the Mo atom is expected. It results in the D_{3d} point symmetry group with trigonal symmetry in which one S-Mo-S unit is in the unit cell within the octahedral coordination [23]. In this phase, one layer of sulfur atoms is shifted compared to the other sulfur layer. The DFT-calculated Mo-S bond length is 2.43 Å, and the Mo-Mo distance is 3.18 Å [24], as shown in fig.3.1 (a). It is worthy to note that, the 1T phase MoS_2 has no band gap and it is a metallic material.

Distorted octahedral phase

Experimentally, under ambient conditions, the 1T phase of 1L-MoS_2 is unstable and usually becomes distorted (the 1T' phase) with a lower symmetry [25–27]. The experimental results for the nearest and next nearest Mo-Mo atom distances are 2.77 Å and 3.78 Å, respectively [25]. However, the DFT results in reference [26] show that the two shortest Mo-Mo distances are 3.07 Å and 3.125 Å and the Mo-S bonds are 2.337 Å and 2.373 Å. This configuration is dynamically metastable and electronically a semimetal [28]. The structure of the 1T' phases of MoS2 is shown in fig.3.1 (b).

Trigonal prismatic phase

Corresponding to the coordination of Mo atoms, the trigonal prismatic phase is referred to as the 1H phase. The structure of the 1H phase 1L-MoS_2 is shown in fig.3.1 (c). From the top view, the 1H phase SC is graphene-like, although instead of one sheet of atoms it has three, with the lattice constants $a = b = 3.167$ Å. In this phase, the Mo atom forms the d^4sp hybridization [29], and thus the 1H phase can be described by the hexagonal symmetry (the D_{3h} group) corresponding to the trigonal prismatic coordination of the metal atoms. It is a semiconductor material with a direct band gap [30–32].

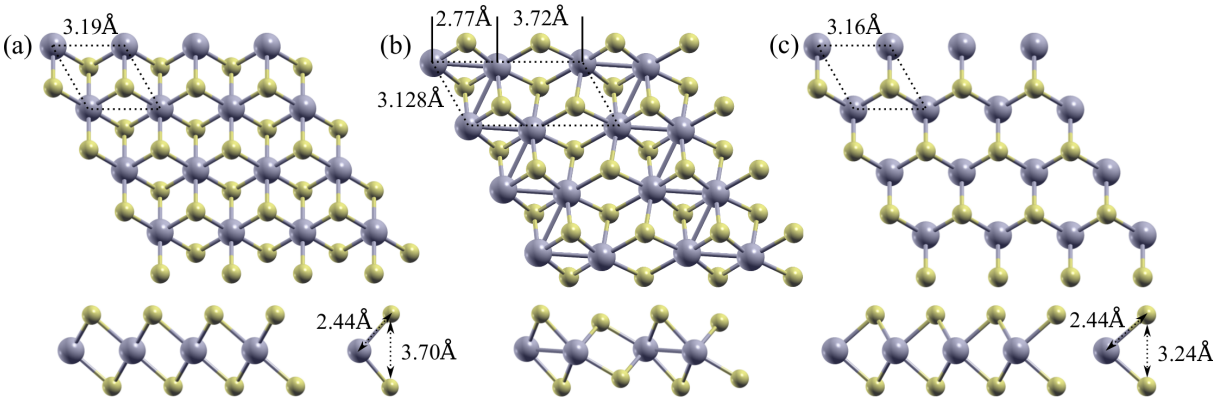

Figure 3.1: Schematic representation of the atomic structure of (a) T phase, (b) T' phase, and (c) H phase of monolayer MoS_2. Black dashed lines show unit cells in the top view. The data of the 1T and 1H phases are from an EP calculation, and that of the 1T' phase is from a DFT calculation.

Table 3.1: Lattice information of H, T and T' phases of monolayer MoS_2. The data labeled (EP) comes from an EP optimization at 0K.

Phase	Mo-Mo: NN (Å)	Mo-Mo: NNN (Å)	Mo-S (Å)	Band gap (eV)
T(EP)	3.19		2.45	metal
T(DFT)[24]	3.18		2.45	metal
1T'(DFT)	2.77	3.128/3.72	2.37	semimetal
T'(EXP)[25]	2.77	3.18	2.34	semimetal
1T'(DFT)[26]	3.07	3.125	2.34	semimetal
H(EP)	3.17		2.44	
H(DFT)[31]	3.16		2.38	1.74
H(DFT)[30]	3.13			1.69∼1.89
H(EXP)[32]	3.14		2.41	1.70

We have summarized the lattice information in table 3.1. One can see that the calculated lattice parameters from EP and DFT are very close to the experimental results. From here on, we focus on the stable semiconducting H phase 1L-MoS_2.

3.1.1 Phonon study from group theory

The H phase 1L-MoS_2 belongs to the D_{3h} group [23]. The character table is shown in table 3.2 [33]. The symmetry operators are: E, σ_h (reflection in a horizontal plane across the Mo atom), C_3 (rotation by 120° about the z-axis), S_3 (rotation by 120° about the z-axis followed by a reflection in a horizontal plane), C_2' (rotation by 180° about the horizontal axis in a vertical S-Mo-S plane), and σ_v (reflection in a vertical S-Mo-S plane).

There are three atoms (1 Mo and 2 S) in a unit cell, thus yielding $3 \times 3 = 9$ phonons for each $\mathbf{q}$ wave vector, where three of them are acoustic, and six are optical modes. The nine vibrational modes at the zone center are: $\Gamma_{\mathrm{BZ}} = 2E' + E'' + A_1' + 2A_2''$, where one $A"_2$ and one E' are acoustic modes. Note that the vibrational modes denoted by E' and E'' are doubly degenerate. From table 3.2 one can see that, the A_1' and E' modes have quadratic form basis functions and are first-order Raman-active. All the vibrational modes of monolayer MoS_2 at the Γ-point are illustrated in table 3.3. The E' mode is

Table 3.2: Character table of the D_{3h} point symmetry group.

$D_{3h} = D_3 \otimes \sigma_h$ $(\bar{6}m2)$			E	σ_h	$2C_3$	$2S_3$	$3C_2'$	$3\sigma_v$
x^2+y^2, z^2		A_1'	1	1	1	1	1	1
	R_z	A_2'	1	1	1	1	-1	-1
		A_1''	1	-1	1	-1	1	-1
	z	A_2''	1	-1	1	-1	-1	1
(x^2-y^2, xy)	(x, y)	E'	2	2	-1	-1	0	0
(xz, yz)	(R_x, R_y)	E''	2	-2	-1	1	0	0

an in-plane mode, containing two perpendicular vibrational modes, which are shown in table 3.3. In this mode, Mo and S atoms move to opposite directions. The A_1' mode is out-of-plane mode, in which Mo is silent, and S atoms vibrate to opposite directions.

Table 3.3: All the vibrational modes of monolayer MoS_2 at the Γ-point. Frequencies related to each mode calculated using DFT and MD. Yellow and purple balls represent sulfur (S) and molybdenum (Mo) atoms, respectively. Arrows are proportional to the displacements and come from the real part of the eigenvectors at the Γ-point.

phonons	three point of views (direct, left, top)
A_2'' (acoustic)	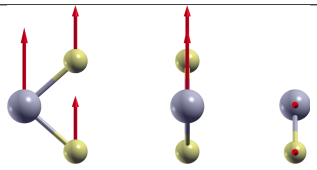
E' (acoustic)	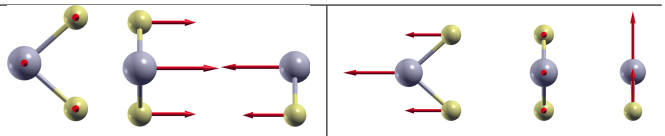
E'' 282.353 cm^{-1} (MD) 283.155 cm^{-1} (DFT)	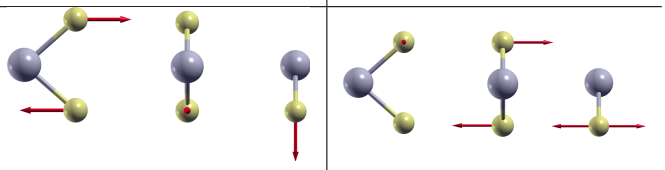
E' (Raman-active) 396.930 cm^{-1} (MD) 383.268 cm^{-1} (DFT)	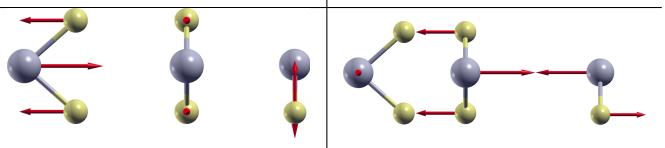
A_1' (Raman-active) 422.478 cm^{-1} (MD) 403.309 cm^{-1} (DFT)	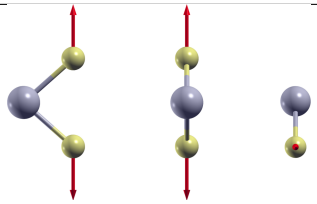
A_2'' 502.235 cm^{-1} (MD) 466.230 cm^{-1} (DFT)	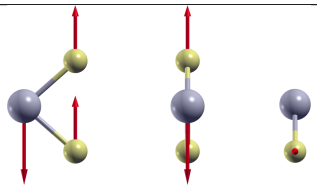

3.1.2 Defects

It is always expected to find defects in crystalline materials since the configurational entropy can overcome the defect formation energy. In this study, we mainly focus on point defects, such as vacancies and antisites. Currently, five kinds of point defects are paid attention to since they frequently appear in the experiments [34, 35]: (i) Mo mono-vacancy (Mo_{vac}), (ii) S mono-vacancy (S_{vac}), (iii) S_2-dimer vacancy ($S2_{vac}$), (iv) S replaced by Mo (Mo_S), and (v) Mo replaced by S_2-dimer (Mo_{S2}). The defect models are depicted in fig.3.2.

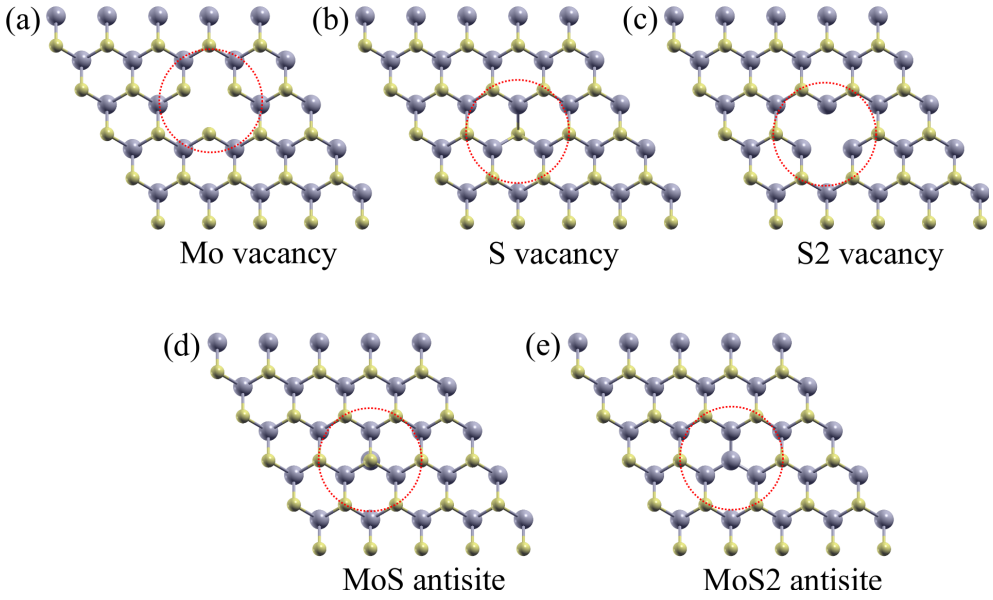

Figure 3.2: (a)-(e): Five structures of defects implemented in 1L-MoS_2 in H phase. Red circles are centered around each defect. Yellow and purple balls represent sulfur (S) and molybdenum (Mo) atoms, respectively.

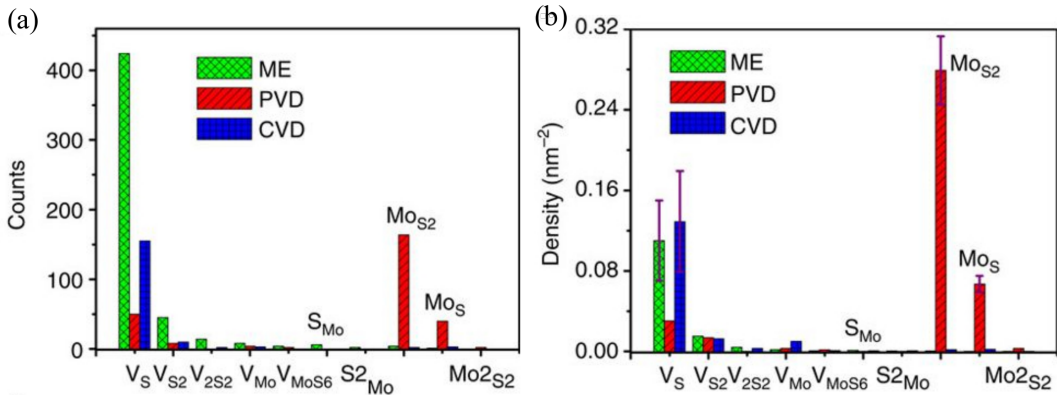

Figure 3.3: Experimental observations of defects, as found in reference [34]: (a) numbers of and (b) concentrations of each type of defects in samples prepared by different methods, mechanical exfoliation (ME), chemical vapor deposition (CVD), and physical vapor deposition (PVD).

Fig.3.3 presents an experimental proof for the existence of various types of defects in 1H phase monolayer MoS_2. It shows that in ME and CVD samples, single vacancies, especially S vacancies are the most common defects, whereas antisites dominate in PVD samples. One needs to note that the defect concentration does not only depend on the fabrication method but also on the defect's formation energy. The formation energies and the stabilities of defective structures were studied using DFT by Komsa *et al.* [36] using EP by Ghorbani-asl [37]. This will be discussed in section 4.2.

3.2 Empirical potentials

Having an accurate interatomic potential is important for describing Raman spectra correctly in defective materials. First, it enables us to find the optimized geometries of defective structures. Then, the restoring forces are calculated for the dynamical matrix. In this study, we exploit the reactive empirical bond ordered (REBO) potential [38] accompanied by the Lennard-Jones (LJ) potential [39] to model atomic interactions. They are implemented in the LAMMPS [40] software, which we use for all calculations in this thesis. Here, we briefly introduce the mentioned potentials.

3.2.1 REBO potential

The REBO potential is used to describe the potential energy of covalent bonds and the interatomic forces in a classical way. It is based on Tersoff's covalent-bonding formalism [41] with additional terms used to correct the inherent overbinding of radicals. This potential needs a very accurate fit of parameters to experimental data. Abell [42] proposed that the chemical binding energy can be written as follows,

$$E_{\mathrm{b}} = \sum_{i} \sum_{j(>i)} \left[V^{R}\left(r_{ij}\right) - b_{ij} V^{A}\left(r_{ij}\right) \right], \tag{3.1}$$

where E_b is the chemical binding energy, the functions $V^R(r)$ and $V^A(r)$ represent interatomic repulsive and attractive interactions from valence electrons, respectively. The parameter r_{ij} is the distance between two nearest atoms i and j, and b_{ij} is a bond order. The forms of $V^R(r)$ and $V^A(r)$ are:

$$\begin{cases} V^{R}(r) = f^{c}(r)(1 + Q/r)A\mathrm{e}^{-\alpha r} \\ V^{A}(r) = f^{c}(r)\sum_{n} B_{n}\mathrm{e}^{-\beta_{n} r} \end{cases} . \tag{3.2}$$

Here, $f^c(r)$ is a selection function to describe the effective force range and r is the scalar distance between atoms. Q, B_n, α and β_n are adjustable parameters. Note that in eq.3.2, the first term is the screened Coulomb function which describes the repulsive pair interaction between the positively charged nucleus and will go to infinity when the distance approach to zero.

The REBO potential is mainly based on classical concepts (not involving electron movement) to describe electromagnetic interactions in the material, and it is heavily related to the experimental data. *E.g.*, eq.3.1 and eq.3.2 need plenty of experimental data to fit the parameters. Thus for different materials, the potential needs different initial data.

3.2.2 Lennard-Jone potential

The weak LJ potential plays the same role as the vdW interaction. It is widely used to describe the interaction between two neutral particles. Mathematically, one can model it as

$$V_{\mathrm{LJ}} = 4\varepsilon \left[\left(\frac{\sigma}{r}\right)^{12} - \left(\frac{\sigma}{r}\right)^{6} \right] = \varepsilon \left[\left(\frac{r_{\mathrm{m}}}{r}\right)^{12} - 2\left(\frac{r_{\mathrm{m}}}{r}\right)^{6} \right], \tag{3.3}$$

where σ is the finite distance at which the inter-particle potential is zero, r is the distance between the particles, ε is the depth of the potential well, and r_m is the distance at which the potential reaches its minimum.

3.3 Density functional theory calculations

We present first-principles calculations using DFT implemented in VASP [43] to crosscheck our classical forces. The exchange-correlation interactions are accounted for using the Perdew-Burke-Ernzerhof (PBE) [44] functional. A plane wave basis with a 550 eV cutoff energy is employed to represent the electronic wave functions. During the structural relaxation of the MoS_2 PC , a $15 \times 15 \times 1$ k-mesh is used. The total energies in both the geometry relaxation and the phonon calculation were converged within 10^{-6} eV and the forces to within 10^{-3} eV/Å. The polarizability tensors for unpolarized Raman spectra [45] were determined with the same parameters as above. A broadening of 4 cm^{-1} was considered for a Gaussian distribution of Raman-active modes. To investigate vibrational properties of defective systems, we make one defect in a $5 \times 5 \times 1$ SC. Note that the defect concentration is computed as the number of defect sites divided by the maximum possible number of defects which can be accommodated in the pristine SC system. For example, in the 5×5×1 SC, the top has one S vacancy, and 50 S vacancies can be made in the pristine cell in total, resulting in the concentration x=1/50=2%. A $3 \times 3 \times 1$ k-mesh is used.

3.4 Phonopy

Phonon spectra are assessed by using the Phonopy code [46] within the finite displacement method. It is an open source package for phonon calculations at harmonic and quasi-harmonic levels, and the calculation method of Phonopy is described in section 2.1.2. In Phonopy calculations, to reduce the calculation cost of force constants, crystal symmetry is used. While calculating, first, a symmetry-reduced set of atomic displacements is generated. Then the set of atomic displacements is expanded using the symmetry.

It is worth to note that Phonopy cannot calculate the unfolded phonon spectra of a SC by itself. To get unfolded phonon spectra over SC BZ, we made a phonon unfolding code (Appendix C) that was constructed to interface with Phonopy.

Chapter 4

Results and discussion

In this chapter, we present our results as follows: (i) we benchmark the performance of EP against DFT potential results, (ii) we monitor the trends of prominent Raman peaks versus defect concentration and then, plot defect-induced spectra, (iii) we analyze the origin of the peak shifts. In particular, we consider the role of strain and mass.

4.1 Reliability of the empirical potential

Having a reliable EP to describe the inter-atomic forces is one of the most important constituents of an classical MD study. To this end, we first calculate phonon dispersion curves of bilayer MoS_2 from EP and then compare them with DFT results. This comparison verifies the quality of the descriptions of both the strong intra-layer ionic/covalent bonds and the weak inter-layer vdW interactions by EP.

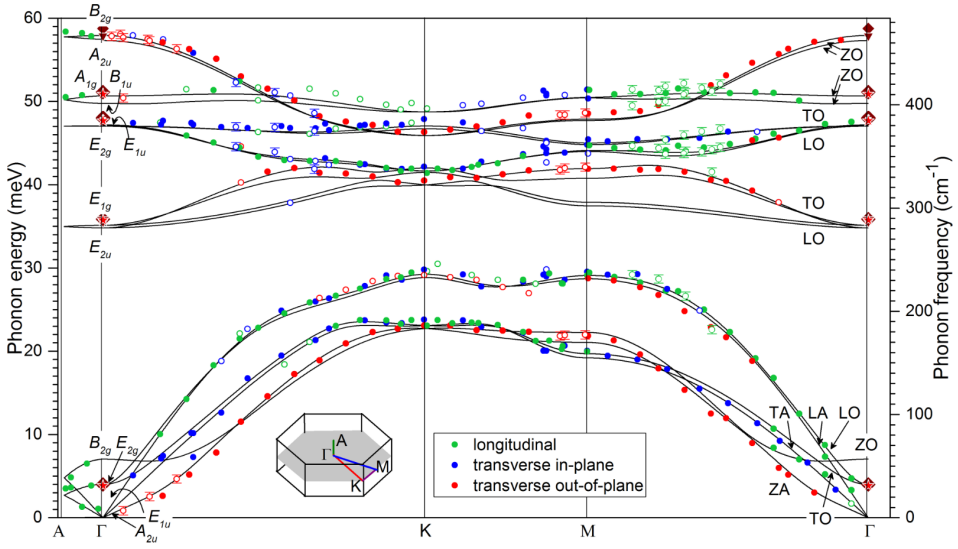

Figure 4.1: Inelastic x-ray scattering measurements and DFT calculations of the phonon dispersion of MoS_2. Circles in green, blue, and red represent measurements probing phonons with an in-plane longitudinal (L), in-plane transverse (T), and out-of-plane transverse (Z) components, respectively . Reproduced with permission.[12] Copyright 2019, American Physical Society

It is already well verified that DFT calculated phonon dispersion curves for 2H phase bilayer MoS_2 match the X-ray data well, as shown in fig.4.1 [12]. As shown in fig.4.2 (a), one finds 18 vibrational modes for bilayer MoS_2 that contains six atoms per PC. Overall, the REBO EP presents a good description of phonon features in the FBZ. At the Γ point, the two low-frequency Raman-active shear and breathing modes are in good agreement with experimental data. At higher frequencies, one encounters the discrepancy between the calculated and experimental values so that the calculated values lay above the experimental points. To improve the frequency of Raman-active modes in comparison to experiment, we multiply the calculated frequency values by a factor of 0.965. (Note that our other results outside this section are not multiplied by this number). The overestimation of the highest frequency IR active modes is not severe due to vanishing contributions into Raman peaks with the exception of the ordered S vacancy on one layer as will be discussed later on.

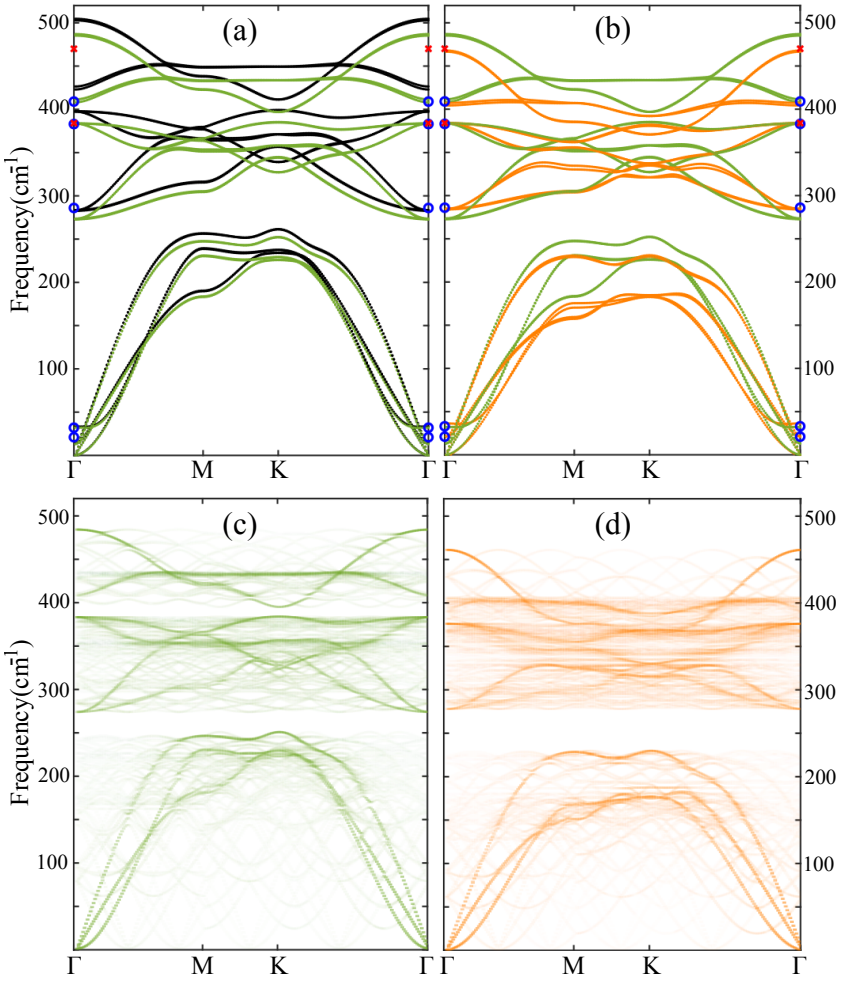

Figure 4.2: Phonon dispersion curves of (a) 2H-phase bilayer (black) and scaled dispersion curve (green) along high-symmetry directions from EP and (b) the comparison of scaled phonon curves (green) and DFT (orange). The unfolded phonon dispersion curve of monolayer MoS_2 of defective 5×5 SC calculated from (c) EP and (d) DFT. Blue dots show Raman-active modes and red stars denote IR-active modes of bulk MoS2 at the BZ center, extracted from inelastic neutron scattering experiments [12].

The vibrational modes away from the Γ point are important in Raman measurements for case of defects. Therefore, we compare phonon dispersion curves of pristine bilayer MoS_2 from EP with DFT calculations in fig.4.2 (b). Obviously, the EP longitudinal acoustic (LA) modes at the high symmetry points, *i.e.*, M and K, have higher frequencies than the corresponding DFT results. These modes will show up in Raman spectra of defective systems. As a second distinct behavior of the EP-phonons with respect to the DFT modes, we point out the curvature of the band of the highest-frequency Raman-active mode (near 405 cm^{-1}). Based on the proven validity of DFT and also the observed phonon dispersion curve of bulk MoS_2 [12], the erroneous EP characteristic can lead to an incorrect broadening of the A_{1g} (A_1') mode in defective systems.

As mentioned before, the study of defects in large scale samples is the primary purpose of applying EP. For this reason, we applied the phonon unfolding method to analyse phonon dispersion curves of defective samples. The unfolded phonon dispersion curves of defective 5×5 monolayer MoS_2 SC using EP and DFT potential are calculated and the results are shown in fig.4.2 (c) and (d). One finds nine intense vibrational modes for monolayer MoS_2 that correspond to the phonons in the pristine PC. Similar to the pristine bilayer, the REBO EP presents a good description of phonon features in the FBZ. We expect that the curvature of the highest-frequency Raman-active band brings a spurious broadening of the A_1' mode.

4.2 Formation energies of defects

The formation energy of a point defect is the energy needed to form that defect, *e.g.*, the formation energy of a Mo vacancy is the energy required to pull a Mo atom out of the system. The more positive the defect formation energy is, the more unlikely its formation. The formation energy is calculated as:

$$E_f = E_{defect} - E_{pristine} + E_{isolated}, \tag{4.1}$$

where E_{defect} and $E_{pristine}$ are the energies of the defective system and pristine system, respectively, and $E_{isolated}$ represents the energy of isolated atoms added or removed upon forming the defects. The contribution of a single atom to $E_{isolated}$ can be considered as the chemical potential of the atom. Note that the $E_{isolated}$ can be chosen as zero in EP calculations. In our calculations, we calculate the formation energies of Mo and S vacancies by modeling the sample as a Mo or S atom pulled out of the pristine SC. Then, we show that the $E_{isolated}$ terms for Mo and S atoms are all zero in EP calculations. We show in fig.4.3 the system energy as a function of the distance between the S atom and the cell surface, which fits the classical potential energy curve. One can notice that there is a metastable state nearby the S top layer of the lattice. In fig.4.3, the isolated S atom is fixed during the optimization. Once the isolated S atom is far away from the lattice (more than 8 Å), the potential energy of system converges to −8586.8894 eV, equal to the potential energy of the S vacancy defective system. Similarly for the Mo vacancy, we gain $E_{isolated} = 0$. In a nutshell, the formation energy for point defect can be written as

$$E_f = E_{defect} - E_{pristine}$$

In Table 4.1, the formation energies for all defect candidates are reported. By comparing

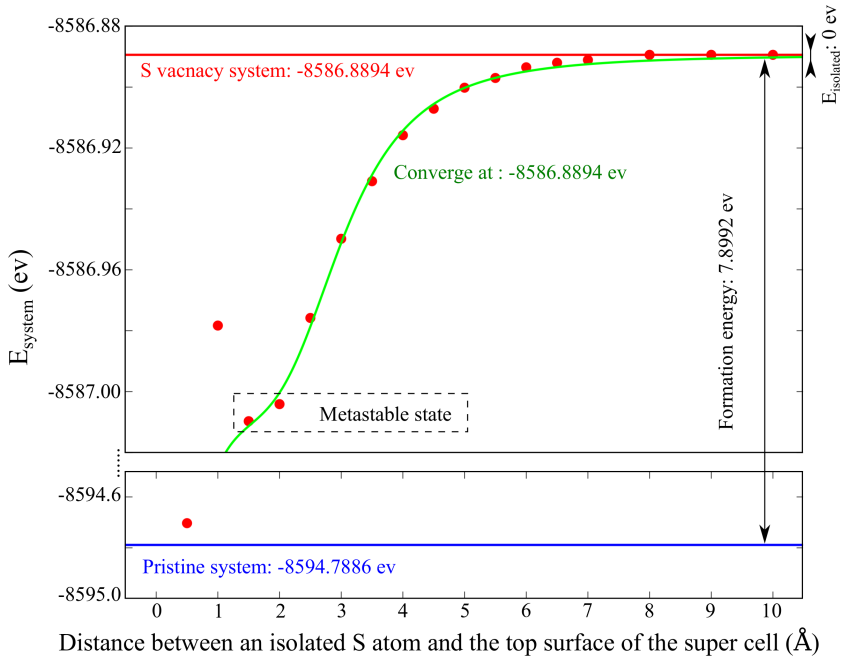

Figure 4.3: Change of the total energy of monolayer MoS_2 when pulling an isolated S atom out of a 20×20 SC.

Table 4.1: Formation energies E_f (eV) for point defects in 1L-MoS_2.

E_f (eV)	S_{vac}	Mo_{vac}	$S2_{vac}$	Mo_S	Mo_{S2}
REBO+LJ	7.8992	16.8457	15.2724	0.4799	9.0756
REBO [37]	7.8964	16.8451	-	-0.0922	6.1018
DFT [37]	6.9684	18.8495	-	-1.9755	7.1787

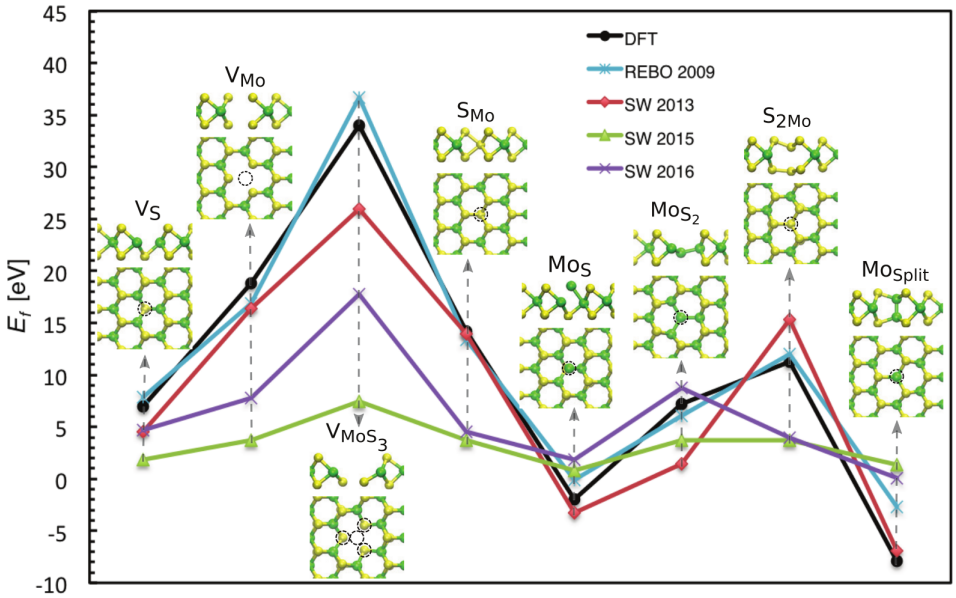

Figure 4.4: Formation energies of point defects calculated using DFT, REBO, and Stillinger-Weber (SW) EP. Reproduced with permission.[37] Copyright 2017, IOP Publishing Ltd.

our results in Table 4.1 and the results from reference [37] in Table 4.1 and fig.4.4, we find out that our results are in a good agreement with reference [37]. As a result, we can make sure that the defects we are studying are indeed point defects with suitable formation energies and one can always find these kinds of defects in experiments. Also, they can be correctly described by REBO EP, thereby assuring their validity in simulations of Raman spectra.

4.3 Raman shifts under defects

In chapter 3, we modeled five kinds of point defects. Next, we study frequency shifts of two prominent (E' and A_1') Raman-active modes for all the defect types while the concentration of defects changes up to about 5%. Note that the frequencies of these mode peaks are the frequencies of the peaks' highest point. Then, we discuss the overall shapes and special peaks of the Raman spectra (RGDOS). As mentioned before, we define the concentration n as the ratio of the number of atoms or dimers removed or added over the total number of related atoms or dimers in the pristine monolayer MoS_2.

We prepare two different kinds of defect distributions: (i) Ordered and (ii) random distributions. It helps us to explore the effect of randomness in a defect arrangement. For the randomly distributed cases, we arrange a corresponding number of defects in a 20×10 parallelogram SC. For each concentration, we calculate the final Raman spectra by averaging over five samples with different random arrangements of defects. Periodic boundary conditions are applied in our calculations. The defects are created on a pristine SC, which has first been fully optimized. The defective structures are optimized with the fixed cell size. Experimentally, the samples are always huge compared to our samples (around $5.5nm \times 3.2nm$), and having a low concentration of defects, they do not experience strain on boundaries. Besides, the samples are either laid on a substrate or suspended. Therefore, such the assumption of the frozen cell size sounds real, at least, in low concentrations of defects.

4.3.1 Prominent E' and A_1' modes

The shifts of Raman peak frequencies are plotted in fig.4.5. As shown, we study the effect of defect arrangement and concentration on prominent modes, at the same time. Overall, (i) the frequency of E' modes decreases (a downshift) with the introduction of defects, (ii) the A_1' mode behaves differently: a downward-shift for Mo_{vac}, a slight upshift for S_{vac} and $S2_{vac}$, and strong upshifts for the both antisites. From the comparison between the ordered and random distributions, one can see that both have the same trend of changes, approximately.

The results match well the experimental data assuming that the majority of the defects are S vacancies [13]. To the best of our knowledge, there are no experiments related to other types of defects to compare our calculations with. Clearly, our results show that for the defects related to Mo atoms A_1' peak reacts to the defects and is not silent anymore. Mo vacancies introduce a red-shift in A_1' of about 3 cm^{-1}. Otherwise, Mo antisites represent strong upshifting. From Table 3.3, the A_1' mode is a out-of-plane mode with silent Mo atoms. Here, we find that the A_1' mode is strongly influenced even by Mo vacancies. To

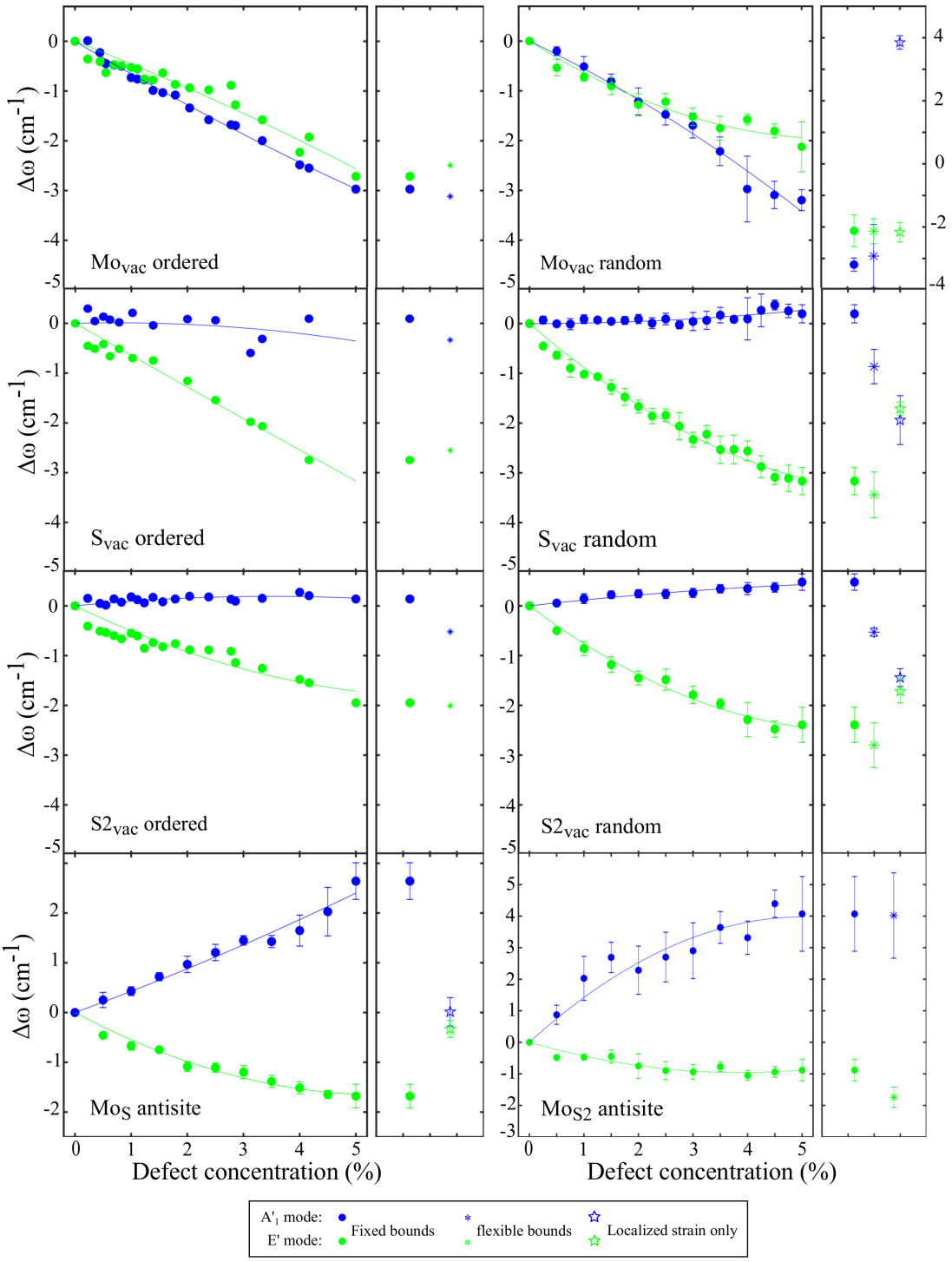

Figure 4.5: Shifts of the two main peaks affected by defects. Ordered and random distributions of Mo, S and S2 vacancies, denoted by Mo_{vac}, S_{vac}, and $S2_{vac}$, respectively, accompanied by two kinds of random distributed antisites; S substituted by Mo (Mo_S) and Mo substituting for S2 (Mo_{S2}). The smaller attached panel shows in each case the comparison of peaks shifts between systems with flexible and fixed cell sizes at the 5% defect concentration.

Table 4.2: Parameters of the fitted curves in fig.4.5. The unit of a and b are $100 \times cm^{-1}$ and $10^4 \times cm^{-1}$, respectively.

Fitted curve: $ax + bx^2$	Mo vacancy		S vacancy		S2 vacancy	
Modes(Ordered)	A_1'	E'	A_1'	E'	A_1'	E'
a	-0.668	-0.4397	0.02998	-0.6458	0.109	-0.5439
b	0.0149	-0.0146	-0.0202	0.0025	-0.0156	0.0402
Modes(Random)	A_1'	E'	A_1'	E'	A_1'	E'
a	-0.5236	-0.6947	-0.0008	-0.9496	0.1243	-0.8278
b	-0.0322	0.0614	0.0109	0.0654	-0.0078	0.0680
Fitted curve: $ax + bx^2$	Mo-S antisite			Mo-S2 antisite		
Modes(Random)	A_1'		E'	A_1'		E'
a	0.4139		-0.6025	1.573		-0.497
b	0.0133		0.0548	-0.1553		0.0643

present the relation between $\Delta\omega$ and the defect concentration (x), we carry out a second order polynomial line fitting; $ax + bx^2$. The resulting parameters are listed in Table 4.2.

It is worth to calculate the effect of the lattice strain arising due to the defects. Once we create a defect, the bonds to the neighboring atoms tend to stretch or shrink. Thus, the whole lattice obtains a strain effect, which we call as the lattice strain. It is most pronounced when the cell is fixed and the defect concentration becomes large. Thus, we consider here only the 5% defect concentration. To study the lattice strain effect we model two systems. First, we calculated the Raman-active modes for systems with fixed bounds (the cell size is fixed) as before. Then, we calculated Raman spectra for the fully optimized systems.

As shown in fig.4.5, in the Mo_{vac} and Mo_{S2} samples the strain affects little on the Raman peak shift. For the S and S2 vacancies, the frequency of the A_1' mode peak without lattice strain (flexible bounds) is a little bit lower than that with lattice strain (fixed bounds). For the E' mode the changes are in the opposite direction.

Another effect defects bring to the system is the localized strain around them. Due to the defects, the strain around the defects and far away from them are different, which makes the bonds around the defects to change and leads to the deformation of the lattice structure. This kind of strain is specific for the defect type, and cannot be eliminated by fully optimizing the sample. We believe that localized strain contributes a lot on the Raman peak shifts. In order to study this effect, several special samples with only localized strain (but no defects on them) were made. *E.g.*, in the case of Mo vacancies, five samples with 5% concentration of Mo vacancies are prepared. After optimization (with the bounds fixed), the vacancies are filled with Mo atoms. Then we do simulations with these samples, and the results will reflect only the effect of Mo vacancies' localized strain. Fig.4.5 shows that the localized strain has a great effect on the Raman peak shift. The E' mode peak always shows a downward shift with all kinds of localized strain conditions, and the A_1' mode peak shifts downward in almost all cases, except for the Mo vacancies.

In order to show the details clearly, in fig.4.6, the RGDOSs for all five kinds of studied point vacancies with concentration form 0 to 5% are plotted. The plotted curves are the

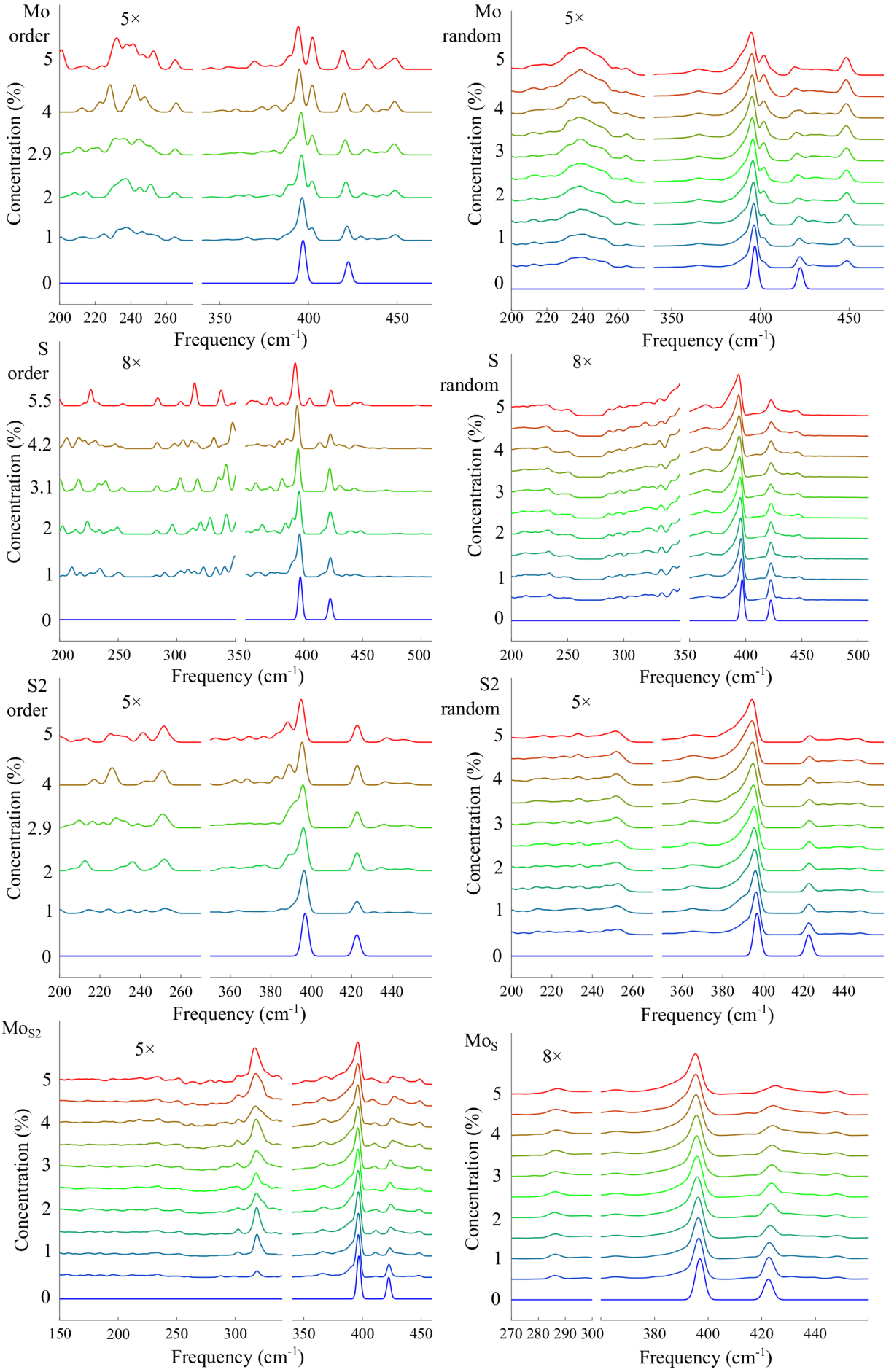

Figure 4.6: RGDOS for five types of point defects with concentrations from 0 to 5%.

averages over random distribution samples with the same defect concentration.

In fig.4.6 one can see that for each kind of defect the two main peaks are always present with high intensities and the shifts of those two peaks can be observed. At the low-frequency region, since the intensities are small, the intensities in each plot are amplified by different values, which are indicated at the left top side of each plot. It is clear that these five types of defects have huge influences on the low-frequency Raman spectra. By comparing the Raman spectra of ordered and randomly distributed vacancies, we found that they are always similar to each other. The difference between them is that the Raman spectrum of randomly distributed vacancies is always smoother than that of ordered distributed vacancies. That is because in the randomly distributed cases, we made an average of five different samples for each concentration. By doing this, the influence of special vacancy distributions will be eliminated. In the case of ordered vacancies, because of the definite distributions, there will be some special characteristics on the Raman spectra that arise from the distribution of vacancies, which makes the shape of ordered vacancies' Raman spectra always "rougher" than those of randomly distributed vacancies.

Besides these main features of the Raman spectra, we found some unique peaks for several specific kinds of defects. *E.g.*, for both ordered and randomly distributed Mo vacancies, there is always a peak at the right side of the E' peak. We called these kinds of peaks "characteristic peaks", and they are more deeply analyzed in the next section. It is worthy to note that for almost all kinds of defects there is a peak at around 450 cm^{-1}, that is a spurious feature brought by the wrong frequencies of the A_1' mode at the edge of FBZ.

4.3.2 Characteristic peaks of defects

Fig.4.6 shows that the influence of defects is not only reflected on the frequency shift of the two main peaks but also results in the appearance of several new peaks. At the low-frequency region, the Raman peaks arise from the longitudinal acoustic branch at the edge of FBZ [47], and at the high-frequency region, some peaks are due to vibrations around the defects and some peaks are due to the unfolded optical branch located at the edge of the FBZ. In order to analyze this further, an RGDOS plot and unfolded phonon dispersion curves from a 5×4 SC with a Mo vacancy are calculated. The results are shown in fig.4.7 (a) where the solid red lines in the RGDOS plot (left) are the intensities of vibrations at the specific frequencies and in the plot of unfolded phonon dispersion curves (right) the transparency of each point is adjusted based on the projection weight between the SC and PC modes. The unfolded plot shows that some k points from the FBZ of the defective SC's unfolded PC will be folded to the Γ point of the SC's FBZ due to defects, as highlighted by the red dash wireframes.

For the Mo vacancy case, we found that there is a characteristic peak near the E' peak, which is the Mo_{vac} peak in fig.4.7 (a). In our calculations, as shown in fig.4.7 (b), this peak comes from the in-plane vibrational mode around the vacancy, and the projection weight between this mode and the E' mode is high. If one combines this result with the main E' peak contribution map of the Mo vacancy in fig.4.11, one can find that these two peaks arise from splitting of the E' vibration into two regions: far from the vacancy and near the vacancy. Consequently, the Mo vacancy divided the E' mode frequencies into two parts. In fig.4.6 one can see that, for all five kinds of studied point defects, this peak

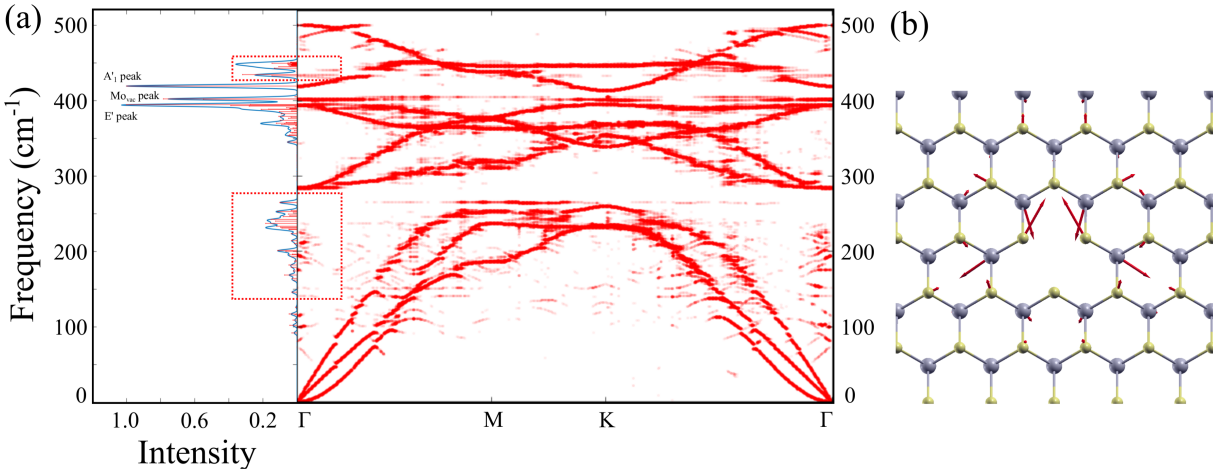

Figure 4.7: (a). RGDOS (left) and unfolded phonon dispersion curves (right) of a 5×4 SC with one Mo vacancy. The red solid lines in the RGDOS plot are the intensities of vibrations at the specific frequencies and the red dashed wire frames show the peaks coming from the M, K, and other points. The unfolding method is mentioned in section 2.3, and the script can be found in the appendix. (b) The vibrations of the Mo_{vac} peak mode. It is a purely in-plane mode, and localized only on the atoms nearby the vacancy; a deformed E' mode.

only exists in the case of the Mo vacancy. Thus, the Mo_{vac} peak in fig.4.7 (a) can be used as an indicator of Mo vacancy defects.

For the S vacancy, we found a peak at around 500 cm^{-1} in ordered samples, which is shown in fig.4.8. However, in our random samples, this peak is too weak to be seen. Since in our random samples, the S vacancies are distributed randomly on both sides of the layer, we considered that this peak shows up only when S vacancies are distributed on one side of the layer.

Through calculations, we found that this peak consists of mostly one vibrational mode A_2'' (see Table 3.3 for illustration of the mode). In order to understand why this mode appears in the Raman spectra of the S vacancy system, we compare systems with different distributions of vacancies on the two sides of the layer and the results are shown in fig.4.8. From fig.4.8 (a) one can see that if S vacancies distribute on both sides of SC, the A_2'' peak almost disappears (blue curve). If S vacancies only exist on one side of the cell, there will be a peak, but its intensity is weak (black curve). The highest A_2'' peak intensity occurs in the ordered distributed S vacancy defect cell (red curve). Fig.4.8 (b) gives the reason why the A_2'' mode can be Raman active for the S vacancy system. When doing the projection of the A_2'' mode with the A_1' Raman active mode (see Table 3.3) in PC, Mo atoms' contribution is always zero since Mo atoms are silent in the A_1' mode. In the A_1' mode the amplitude vectors of the two S atoms are in the opposite direction, but in the A_2'' mode they are in the same direction, and thus the projection of the S atom pairs is zero as well. On the other hand, in the S vacancy systems, *e.g.*, in fig.4.8 (b), since there is a lack of one S atom on the top layer, and the corresponding S atom on the bottom layer is not silent, the projection between the A_1' and A_2'' modes is non-zero which results in the appearance of a A_2'' peak.

Fig.4.8 (c) shows why, with a similar concentration the randomly distributed S vacancy

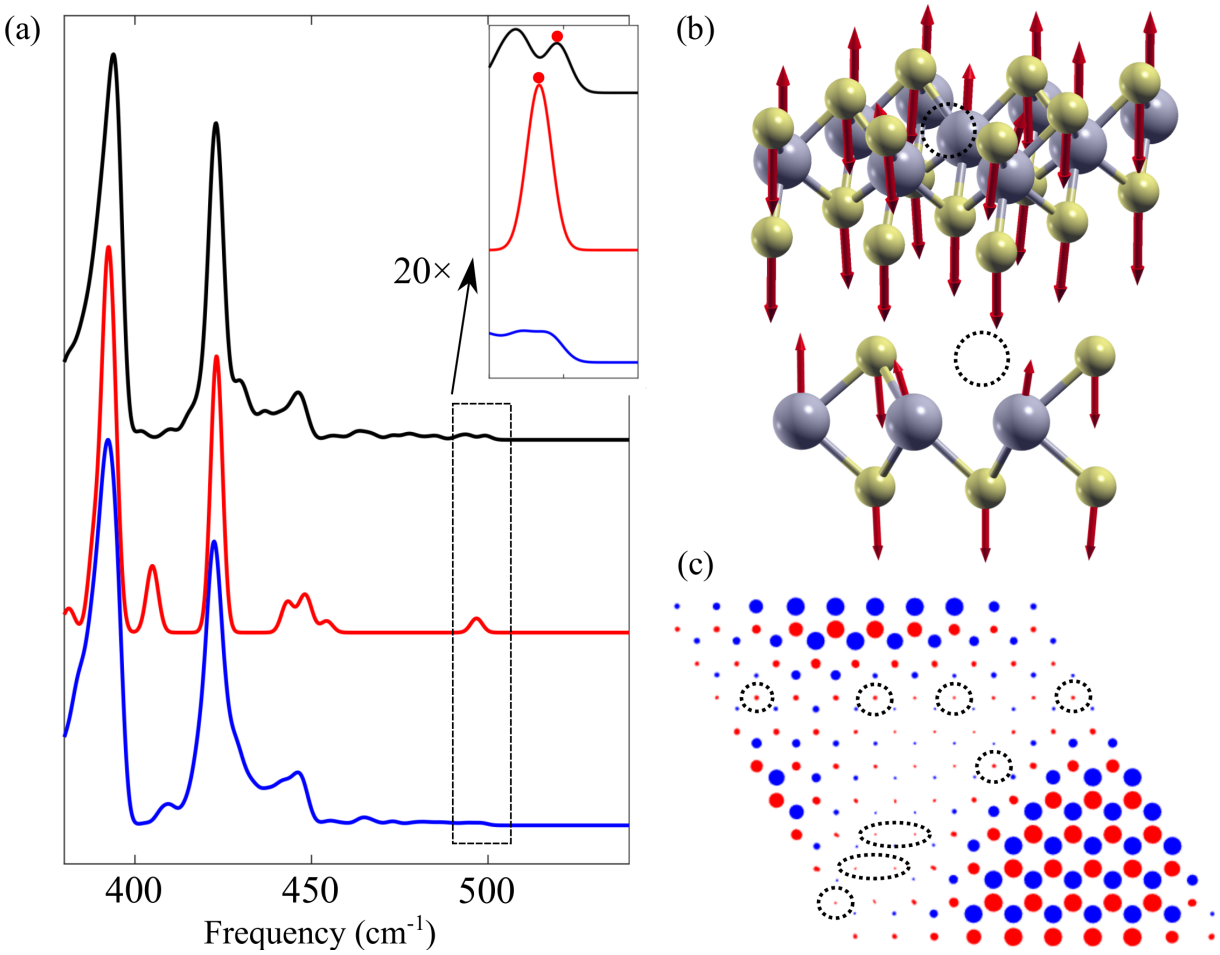

Figure 4.8: (a) RGDOS of monolayer MoS_2 with S vacancies: the black curve is for a 10×10 SC with 5% of S vacancies distributed only on the top side of the layer, the red curve is for a 3×3 ordered S vacancy cell (concentration: 5.6%), and the blue curve is for a random S vacancy (on both sides of the layer) cell with a concentration of 5%. The A_2'' mode peaks which are used in plotting (b) and (c) are marked by red dots. (b) The overall and side view of the 3×3 S-defect structure. (c) The A_2'' vibration intensity of each atom in the 10×10 SC with 5% of S vacancies distributed only on the top side of the layer. The dashed circles in (b) and (c) show the positions of the S vacancies.

system (only on the top layer) has a smaller A_2'' peak intensity compared with the ordered S vacancy system. When vacancies are distributed randomly, some of them are always close to each other and the localized strain effect reduces the amplitude in the corresponding S atom on the bottom layer, thereby making the projection between the A_2'' and A_1' modes small. Note that in fig.4.8 (a) the black curve has two peaks within the frequency range 490-500 cm^{-1}. Both of them belong to the A_2'' mode family. The peak marked with a red dot contains one mode, and the other peak contains two modes with smaller weights. For these two peaks, we calculated ten groups of different samples and found that they all have similar peaks.

4.4 Lattice strain effect

In order to understand why point defects can affect the Raman peaks, some reasons are considered. The first effect we consider is the strain effect of the whole lattice due to the defects, which we call the lattice strain. In the previous section, we mentioned that defects would cause lattice strain if the SC size is fixed. In this section, the relationship between the Raman peak shift and the lattice strain effect is studied. First of all, the unit cell is fully optimized to make sure that the whole system is in its most stable state. Then the unit cell is stretched biaxially in the x and y directions. The strain rate is defined by the following equation:

$$R^i = \frac{(L^i_{stretch} - L^i_{initial})}{L^i_{initial}} \times 100\%, \tag{4.2}$$

where R^i is the stretch rate along the i (x or y) direction, $L^i_{initial}$ is the initial unit cell

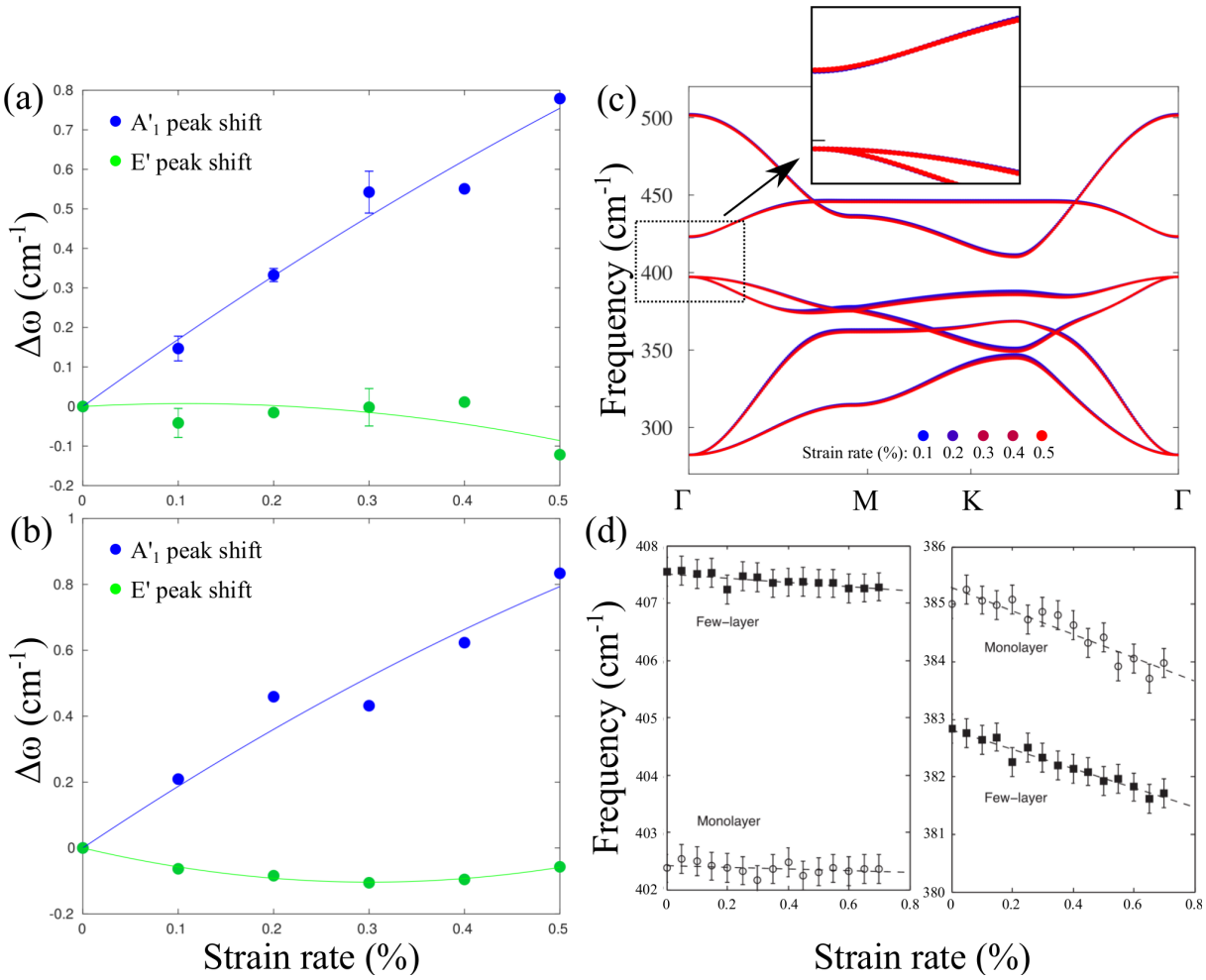

Figure 4.9: (a) Frequency shift by the strain effect for PC. (b) Frequency shift by strain effect in the 10×10 pristine SC. (c) Optical branch of phonon dispersion curves for PC with strain (stretch) rate from 0.1% to 0.5%. (d) Experimental data of the A'_1 peak shifts (left) and E' peak shifts by the strain (stretch) effect. Reproduced with permission.[48] Copyright 2013, American Physical Society.

length, and $L^i_{stretch}$ is the unit cell length after the stretch. After the stretch, the unit cell is optimized again with the cell size fixed. In order to make sure that the results are independent of the SC size, similar calculations for 10×10 pristine SC are done at the same time. The Raman peak shift results are shown in fig.4.9.

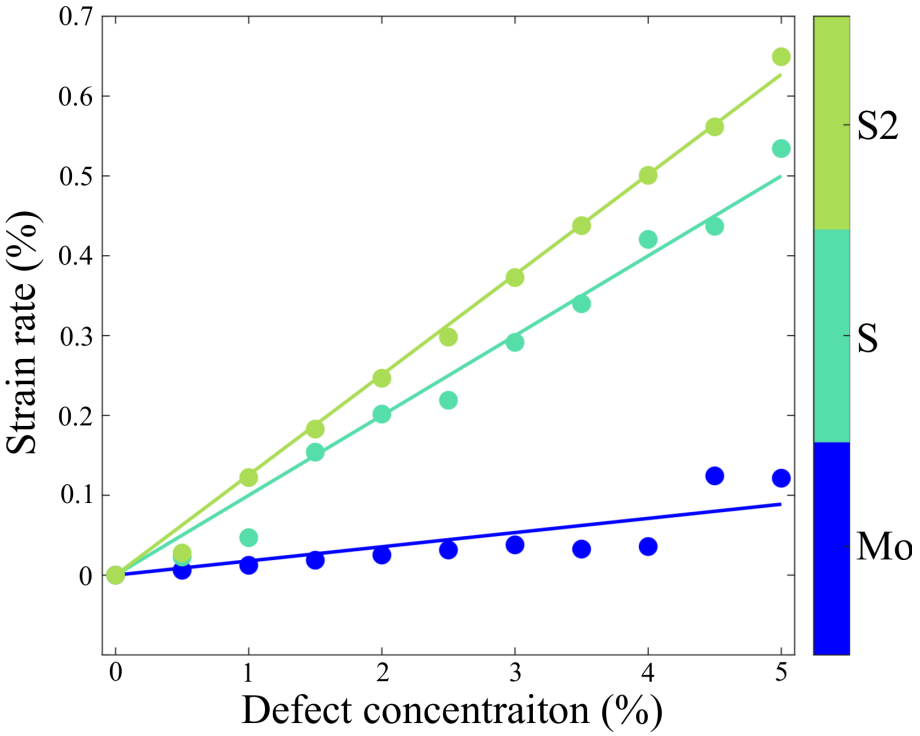

Figure 4.10: Relationship between the defect concentration and the strain rate of SCs for three kinds of vacancies.

Fig.4.9 shows that the results of the lattice strain effect calculated by our method are different from the experimental results [48]. Considering that the performance of EP at the high-frequency area is not accurate, we can say that this difference is because of the potential we used. Considering that the EP results for the Raman peak shift in the presence of S vacancies match the experimental data, as shown in fig.4.5, the lattice strain effect is not enough to explain the whole shift. In order to prove this point of view, the lattice strain rates brought by vacancies are calculated. Fig.4.10 shows that the biggest strain rate caused by vacancies at the 5% concentration is smaller than 0.7%. Note that we did not show the lattice strain rate brought by antisites in fig.4.10. This is because EP cannot optimize these antisites correctly (in this thesis the antisites are optimized by another method). The average lattice strain rate of stable samples with 5% of Mo-S2 antisites is around 0.29%. It means that with our method the lattice strain effect of defects can cause at most around an 1 cm^{-1} blue shift of the A'_1 mode. Combined with results from fig.4.9, the results from fig.4.10 match fig.4.5 well. One can see from fig.4.5 that the influence of the lattice strain effect is not significant enough to change the whole Raman shift tendency. Based on this factor, we can say that the lattice strain effect brought by defects is not the main effect for the Raman peak shift, and the results for Raman peak shifts calculated by EP are still credible. However, the errors it brings cannot be ignored.

4.5 Localized strain effect

The strain effects caused by defects are not only the lattice strain we mentioned in the last section. In fact, once the defective system is fully optimized, there are still a strain effect around the defects, which is called as the localized strain in this thesis (*i.e.*, the variations in the local strain across the SC). Since the lattice strain effect is not the main effect for the defective SC's Raman peak shift, the localized strain effect is considered. Two set of calculations were carried out to clarify how the localized strain influences the Raman peak shift of the two main peaks. First, we removed the defects in the SC, but retained the localized strain caused by defects. Second, we plotted each atom's vibration amplitudes corresponding to the modes around the main E' and A_1' peaks in the defective system. The results for the first task were already shown in fig.4.5, which illustrated that the localized strain effect can be one of the most important effects for the Raman peak shift. In this section, the amplitudes of the Raman modes at the main peak positions on each atom $v(j,0)$ (j represents the jth atom, 0 means at the Γ point) is examined. Note that $v(j,0)$ is an element of the normalized amplitude matrix $\mathbf{e}(\mathbf{q},\nu)$ in eq.2.11.

In this work, six 20 $\times$ 20 samples are prepared. One for each specific point defect. After optimization, the lengths of every Mo-S bonds are compared with the PC Mo-S bond. By doing this one can easily visualize the localized strain effect by coloring the stretched and compressed bonds. The visualized localized strain effect by all six types of defects are shown in the fig.4.11 middle column.

In order to identify how localized strain affects the Raman active vibrations, the amplitudes of the two Raman modes on each atom are determined. By doing the projection with Raman modes of PC at the Γ point using eq.2.18, we can get all the isolated Γ Raman active modes of each sample with their weights ω_{ij}. The RGDOS curves in above figures are plotted by calculating the weighted isolated Γ Raman active modes using the Gaussian function:

$$I_f \sim \sum_{\nu} |\omega_\nu|^2 \cdot e^{-\frac{(f-f_\nu)^2}{2\sigma^2}}, \tag{4.3}$$

where I_f is the Raman intensity for a specific frequency f whose value is in the range of $0 \sim 500$ cm^{-1}, ν is the Raman mode index, ω_ν is the weight of the Raman active mode with the frequency f_ν, and σ is the Gaussian broadening. In this thesis, σ is always 1.67 cm^{-1}. We note that since there are always several modes with similar frequencies at the peak position, the RGDOS peak frequency is always a bit different from the frequency of the Raman mode with the highest weight. Thus, to obtain the amplitude of a RGDOS peak, we need to sum up the square of amplitude eigenvectors of Raman modes around the peak with the weight ω_ν, *i.e.*,

$$u(j)^2 = \sum_{\nu} |\omega_\nu|^2 \cdot u(\nu,j)^2. \tag{4.4}$$

Above, j is the atom index. The range of the modes' frequencies is limited as $f_{RGDOS\,Peak} \pm \sigma$. where $f_{RGDOS\,Peak}$ is the frequency of the RGDOS peak. Thus we can plot the strength of amplitude $u(j)$ of each atom in SC. The value we used is the norm of $u(j)$, in other words, the length of the amplitude vector. The results are shown in fig.4.11 on the left

and right sides where the sizes of dots represent $u(j)^2$. Note that the sizes of dots are normalized in each subplot and they are not absolute.

The results show that the E' Raman mode peak is heavily influenced by the localized strain, especially along the y direction(the column direction of the plot), we believe that is mainly because of the symmetry and the vibration direction of the E' mode. But the defect type affects a lot as well, *i.e.*, the localized strain range of the Mo-S antisite is bigger than that of the Mo vacancy, but the influence range of the E' mode by the Mo-S antisite is smaller than that of the Mo vacancy. And for the Mo-S2 antisite, the distribution of E' mode intensity matches the strain condition well.

One also needs to note that for all the vacancies and the Mo-S antisite the E' Raman modes show huge red shifts, and they always split into different ranges of frequencies. As we can see from fig. 4.11, in the main E' peak frequency range, the vibrations of atoms far away from the defects have the biggest contributions. And because of the strain effect, the E' mode vibrations of atoms near the defects have different ranges of frequencies. Thus we can not find them at the main E' peak frequency. And for the Mo-S2 antisite, since this kind of defect doesn't have such a heavy influence on the E' mode, we can find that in the main E' peak frequency area all atoms contribute.

For the A_1' mode the localized strain plays a major role in the case of the Mo vacancy and the Mo-S2 antisite. One can see that for these two different defective samples, the A_1' mode amplitude strength shows a gradual shift from the defect area to area far from the defect. And it is obvious that there is no directionality in the shift. Similar to the E' mode, this can be explained by the vibration direction of the A_1' mode as well. *I.e.*, for the A_1' mode vibrations are out of plane and there is no differences between different directions on the plane. With respect to the S2 vacancy, the defect's localized strain doesn't have a big influence on the A_1' mode. The amplitude strengths of the atoms around the defect are a bit higher than those of atoms far away from the defects. But in general, the contribution of every S atom is similar, which proves that the effect of the S2 defect has little influence on the A_1' mode. Regarding to the S vacancy and the Mo-S antisite, since the symmetry is heavily broken, the total masses of the top and bottom S layers are no longer the same. To keep balance, some Mo atoms need to be excited. But the distribution of Mo atoms which contribute in the A_1' peak shows a special rhythm. We think that this phenomenon is caused by a wave with a special wavelength (coming from the k points far away from the Γ point). However, further studies need to be done to clarify the mechanism.

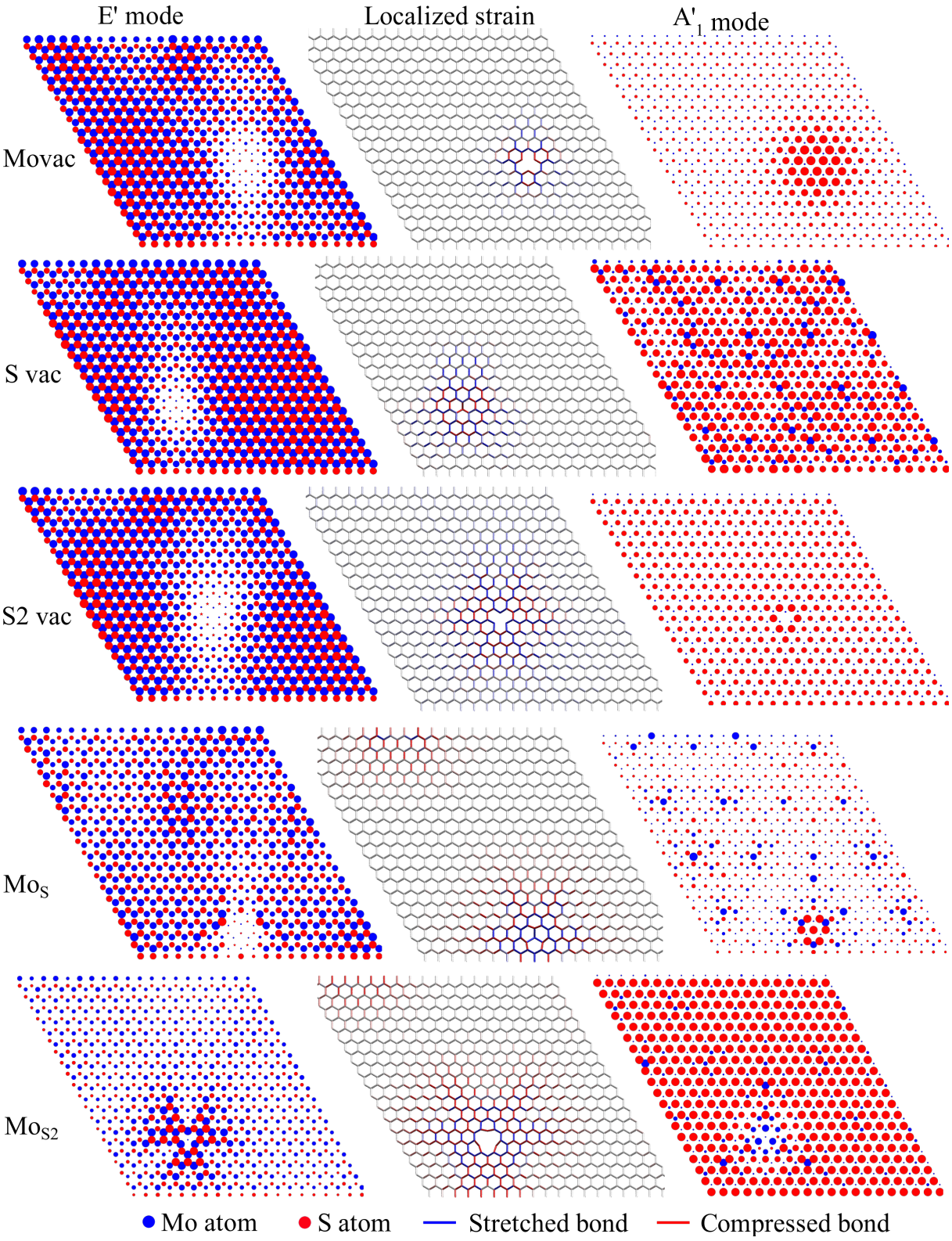

Figure 4.11: E' and A_1' modes at the Γ point and the strain for defective MoS_2. The diameter of a dot is proportional to the vibrations amplitude of the corresponding atom.

4.6 Mass effect and models for the Raman peak shift

In this section, models describing the A_1' and E' modes at the Γ point are built based on the mass effect. The models are simple and account for just mass and force (with a little part of the strain effects). The models are based on the harmonic part of the potential and involve fairly drastic approximations. Thus, they cannot accurately reproduce the shifts of Raman mode peaks, but they reproduce the tendencies and match the results obtained in section 4.3.1.

4.6.1 Model for the A_1' mode

Since at the Γ point the A_1' mode is an out-of-plane mode (see Table 3.3) in the pristine SC, every atoms in the same layer share the same movement. Thus, one can treat one layer of atoms as a whole. In this model each layer moves as a whole whether there are defects or not. Thus we used three balls to represent the three layers, and the bonds between the balls represent all the bonds between the Mo-S or S-S layers as shown in fig.4.12.

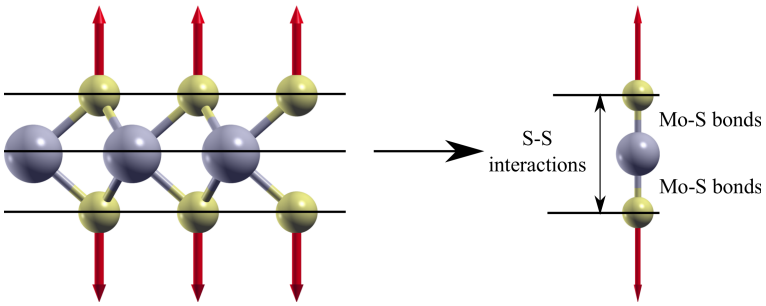

Figure 4.12: Representation of three layers of atoms by three balls. The bonds and interactions in the right figure are summations of the related bonds and interactions between the layers in the left figure.

For pristine monolayer MoS_2, since the mass of a Mo atom is three times as big as the mass of a S atom (96 vs. 32), we set our model's top and bottom ball (representing the top and bottom layer of pristine system, we call them S balls) masses as m and the middle ball (the Mo ball) mass as $3m$. The force constant of the Mo-S bonds is k_{MoS}, and for S-S interaction it is k_{SS}. Moreover, we set the A_1' mode frequency of the pristine system as $\omega_1 = 422.478\ \mathrm{cm}^{-1}$, and for the defective system it is ω_2. Because in the pristine system in the A_1' mode the Mo ball is silent, we can write the equation of motion for S balls as

$$m\ddot{u} = k_{MoS} \cdot u + k_{SS} \cdot 2u, \tag{4.5}$$

where u has the form of $u = A \cdot e^{i\omega_1 t}$. Thus, we will have

$$m\omega_1^2 = k_{MoS} + 2k_{SS}. \tag{4.6}$$

To determine the values of k_{MoS} and k_{SS} we built a special kind of the Mo-S structure which has only the middle Mo and bottom S layers. After optimization, we found that the Mo-S distance change is extremely small, so that we assume that the force constant of

the Mo-S bonds does not change. Next we choose the out-of-plane mode of this structure (frequency: ω_2=455.120 cm^{-1}) in which the amplitude of the S layer is three times as big as that of the Mo layer. Now if one uses our model to describe this system there are only two balls and the Mo-S bond remain, which is a trivial system. Whether it is Raman active or not, one can use our model to write the equation of motion for the both balls, and get the result as

$$k_{MoS} = 0.75m\omega_2^2. \tag{4.7}$$

Thus, with eq.4.6 and eq.4.7 we obtain $k_{SS} = 0.064815m\omega_1^2$.

S and S2 vacancies

In the case of the S and S2 vacancies, we assume that vacancies distribute evenly in both the top and bottom S layers. Once we set a concentration, *e.g.* 5%, in our model, the masses of S balls will be $0.95m$. At the same time, due to the breaking of bonds during the formation of these defects, the force constants will be $0.95k_{MoS}$ and $0.95k_{SS}$ as well. Now consider the localized strain. To make the calculation easy, we only considered the strain effect only on the nearby atoms, and we assume that the force constant has a linear relationship with the bond length (it comes from the harmonic term of the potential so that this assumption is reasonable). Through the calculation we found that the strain gives a 0.0165% increment for both k_{MoS} and k_{SS}. Thus, the force constants of the Mo-S and S-S bonds are $0.950165k_{MoS}$ and $0.950165k_{SS}$, respectively. Then, the motion equation will become as

$$0.95m\omega_2^2 = 0.950165k_{MoS} + 1.9033k_{SS}. \tag{4.8}$$

Together with the values of k_{MoS} and k_{SS} we get $\omega_2 = 0.99913169\omega_1$, which means in our model for the 5% concentration of S and S2 vacancies that the A_1' mode frequency shift is only around -0.36 cm^{-1}, which matches our simulation results. Through the above calculations one can see that since the masses of the S balls share a similar reduction rate with the Mo-S bonds, the influences due to the two reductions almost cancel each other. This can be considered as an explanation of why the A_1' mode is silent for the S and S2 vacancy systems.

Mo vacancies

In this section we set the concentration of Mo vacancies to 5%. Using a similar way as before we calculated the force constants and they became $0.95213k_{MoS}$ and $1.00213k_{SS}$. The mass of the Mo ball became $0.95\times3m$. Using the motion equation one can gets

$$m\omega_2^2 = 0.95213k_{MoS} + 2.00426k_{SS}. \tag{4.9}$$

Note that the Mo ball is silent, and one can only write the motion equation for S balls taking into account their masses did not change. Finally we get the result $\omega_2 = 0.979087\omega_1$ which means for the 5% concentration of Mo vacancies that the A_1' mode frequency shift in our model is around -8.84 cm^{-1}. It gives a tendency which explains the A_1' peak behavior of the Mo vacancy system in fig.4.5. Compared with the calculations in the last section, the main difference for Mo vacancies is that the reduction of the Mo-S bonds

cannot be canceled out by the reduction of the Mo ball's mass. Thus, for Mo vacancies, the reduction of the Mo-S bonds is the main reason for the A_1' peak shift.

4.6.2 Model for the E' mode

At the Γ point the E' mode is a perfect plane wave and the Mo atoms' wave vector is opposite to the S atoms' wave vector, as shown in Table 3.3. Thus, one can consider the 1D crystal chain which is mentioned in section 2.1.1. Here we can build a chain model which contains two different kinds of balls, one representing all Mo atoms and the other all S atoms. There are two different bonds as well, the Mo-S bond (bond_1) and the S-Mo bond (bond_2). Those two bonds represent all the bonds in the lattice. The whole model is shown in fig.4.13.

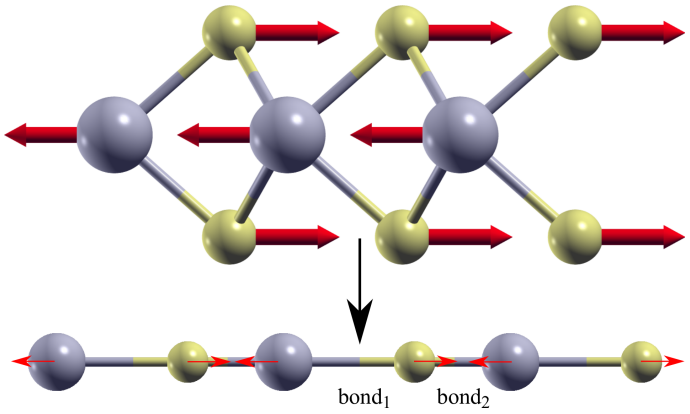

Figure 4.13: The model of the E' mode. The structure of the model is in the bottom figure, the blue balls represent Mo atoms and the yellow balls represent S atom pairs.

Similarly to the last section the mass of a S ball is $2m$ (the amount of S atoms is two times that of Mo atoms) and the mass of the Mo ball is $M = 3m$. We set the force constant of bond_2 as k and that of bond_1 is easily obtained as $\sqrt{3}k$. For the pristine system, using a similar way as that of forming eq.2.7, we found the phonon dispersion relation of the E' mode as (Note the force constants are different)

$$\omega_1^2 = (1+\sqrt{3})k \cdot \frac{1}{3m} + (1+\sqrt{3})k \cdot \frac{1}{2m}. \tag{4.10}$$

For the pristine system the E' mode frequency is $\omega_1 = 396.930 cm^{-1}$.

S and S2 vacancies

We still assume that vacancies are distributed evenly on both the top and bottom S layers with the 5% concentration. Thus, in our model the mass of the S ball is $0.95 \times 2m$. For the both bonds the force constants were reduced by 5%. Then considering the strain effect on the nearest atoms around the defect contributed 0.33% to the force constants. Thus, eq.4.10 for S and S2 vacancy systems can be written as

$$\omega_2^2 = (1+\sqrt{3}) \cdot 0.9533 \cdot k \cdot \frac{1}{3m} + (1+\sqrt{3}) \cdot 0.9533 \cdot k \cdot \frac{1}{0.95 \cdot 2m}. \tag{4.11}$$

Using the equation one can easily get $\omega_2 = 0.99167\omega_1$ which means that the E' mode frequency at the 5% concentration of S or S2 vacancies has a around -3.3 cm^{-1} shift. This result matches the Raman peak shift results in fig.4.5 very well. Eq.4.11 shows that unlike in the case of the model for the A_1' mode, the reduction of masses can now only cancel a part of the reduction of bonds. Therefore, the reduction of bonds is the main factor for the shift of the E' mode in S and S2 vacancy systems.

Mo vacancies

For the Mo vacancy system with a concentration of 5%, the mass of Mo ball is $0.95\times3m$ in the model. If one considers the strain effect around the vacancies the force constants need to be multiplied by 0.9497. Thus, eq.4.10 for the Mo vacancy system is

$$\omega_2^2 = (1+\sqrt{3})\cdot 0.9497\cdot k\cdot\frac{1}{0.95\cdot 3m} + (1+\sqrt{3})\cdot 0.9497\cdot k\cdot\frac{1}{2m}, \tag{4.12}$$

and we get $\omega_2 = 0.9847\omega_1$. This means that for the Mo vacancy system with a concentration of 5% the E' mode peak shifts -6.06 cm^{-1}. Although this shift does not match the result in fig.4.5, it can explain why the E' mode peak frequency has a redshift for Mo vacancy system. Moreover, this shift is smaller compared with the A_1' mode shift of -8.84 cm^{-1}, which can be observed also in fig.4.5. Similar to the last section, for Mo vacancies, the reduction of masses can only cancel a part of the reduction of bonds. Thus the reduction of bonds is the main factor which causes the redshift of the E' mode.

Although the models which are shown in this section are simple and cannot give accurate values of the Raman frequency shifts, they have shown that they can explain the shift tendencies efficiently. From these models, one can see that the influences of mass and bonds can be considered as the major reasons for Raman peak shifts. The inaccuracy is mainly because these models cannot describe the strain effect correctly. In fig.4.11 one can see for the E' mode around the main E' peak frequency that some atoms around the defect are silent. For the A_1' mode some defects have huge influence on the mode whereas some of them have just little influence. The influences brought by the strain effect increase the complexity of the mass effect and the changes of bonds' force constants make the prediction of accurate values by these simple models impossible. Another factor is that these models are based on the assumption that defects are evenly distributed so that they cannot tell about the influence of the defect distribution in situations which are profoundly affected by strain. Note that the results calculated in this section cannot be simply added to the localized strain effect caused Raman peak shift results in fig.4.5 because the relationship between them is complicated.

Chapter 5

Conclusions

In this work, we used EP for Phonopy calculations and RGDOS to represent the first-order Raman spectra of monolayer MoS_2. We showed that EP provides a fast and accurate calculations, and the RGDOS simulation method is fast and accurate for Raman spectroscopy studies. The CPU time spent on modeling 5×5 SC when using EP is usually less than an hour while a corresponding task will cost around days in a DFT calculation. Although the phonon relations calculated by EP are not as accurate as DFT results, they are still in an acceptable range. The phonon dispersion curves made by EP and DFT calculations are similar for both the bilayer MoS_2 and monolayer MoS_2. It means that the phonon behavior calculated by EP and DFT are similar. Based on this one can say that EP is reliable. However, in chapter 4 we also pointed out that because of the qualitative difference of the A_1' branches between the EP and DFT calculations, there might be spurious Raman peaks when the system is defective.

By using EP we calculated the formation energies of all the defect considered in Raman simulation. The results are compared with those from DFT calculations, and they match to each other well. Through this work we showed that the Mo vacancy, the S vacancy, the S2 vacancy, the Mo-S antisite, and the Mo-S2 antisite are all stable defects and they are easy to form because their formation energies are in a suitable range.

One of the most important parts of this study is to find out the relationships between the Raman peak shifts and the concentrations of the different defects. The results show that for the S and S2 vacancies, the A_1' mode peaks are stable and do not shift much, but for other defects the A_1' mode peaks always shift with the concentrations of defects. Moreover, for all studied point defects the E' mode peaks show downward shifts with increasing defect concentrations. We showed that the mass effect and the loss of bonds are two of the most important effects for the Raman peak shifts by using several models. Although the models are simple, they can give correct tendencies and nearly accurate data for different kinds of defects. The localized strain effect is shown as a significant effect related to the Raman peak shifts as well. The influence of it is mainly through changes of bond length resulting in changes in bond force constants, and finally in changes in the dynamical matrix of the whole system. The most important reason why our models cannot predict accurate values of Raman peak shifts is that it cannot describe the localized strain effect accurately.

We showed that the lattice strain effect has a little influence on Raman peak shifts. The influence of the lattice strain effect on Raman peak shifts calculated by EP is different from experimental results. Considering that the performance of EP at the high-frequency area

is not accurate, we can say that the difference between experimental result and the result about lattice strain effect in this thesis is because of the potential used. Fortunately, since this effect is not important for the Raman peak shift phenomenon in defective systems, the results calculated by our method are still believable.

Besides the two well known main peaks of monolayer MoS_2 other peaks appear in defective systems. For the Mo and S vacancies, we reported unique peaks called as characteristic peaks. For the Mo vacancy, we found a characteristic peak near the E' main peak and we found that it comes from the E' vibrational mode around the vacancy. It means that bond length changes around the vacancy caused by the localized strain effect splits the E' mode into two parts with different frequencies and different ranges in the real space.

For S vacancy systems, we found a characteristic peak at near 500 cm^{-1}. It appears only when S vacancies reside only on one side of the monolayer. The results show that the appearance is mainly because the projection between the $A"_2$ and A'_1 modes is no more zero. Once S vacancies are distributed evenly on both side of the monolayer, this projection approaches zero again, and the characteristic peak disappears. For randomly distributed S vacancies on one side of the monolayer, their clustering cause a significant localized strain effect which inhibits the nearby atoms' vibrations and thus the appearance of the characteristic peak. In conclusion, with this peak one can gain information about the distribution of S vacancies in a monolayer MoS_2.

In total, this thesis showed that using EP to do first-order Raman spectroscopy simulation is fast and has enough accuracy, and RGDOS is suitable to represent the Raman spectra of the studied material. The defect type and their concentration can affect the two main Raman peaks' frequencies profoundly. The mass effect and the loss of bonds by defects are considered as the main reasons for the Raman peak shifts. The localized strain effect is an important factor which affects Raman peak shifts and the formation of new Raman peaks heavily. With particular kinds of defects, there will be unique characteristic peaks which give the information about the defect type, concentration, and distribution.

This work provides an easy and economical way to do first-order Raman spectroscopy simulations, which will help researchers reduce the simulation time and resources. It helps to recognize fingerprints in defective monolayer MoS_2's Raman spectroscopy and it gives a better understanding of relationships between vibrational modes, phonons, and defects. Thus, by using the results of this work, one might easily measure the defect types and their concentrations in monolayer MoS_2 by comparing Raman spectra with our results. However, there are still some issues that need to be solved. First, the accuracy of our method is still not enough. Second, this method cannot describe the influence of the lattice strain effect correctly. In order to solve these problems, theory and method improvements still need to be done.

Bibliography

[1] Wenzhong Bao, Xinghan Cai, Dohun Kim, Karthik Sridhara, and Michael S Fuhrer. High mobility ambipolar mos2 field-effect transistors: Substrate and dielectric effects. *Applied Physics Letters*, 102(4):042104, 2013.

[2] Dattatray J Late, Bin Liu, HSS Ramakrishna Matte, Vinayak P Dravid, and CNR Rao. Hysteresis in single-layer mos2 field effect transistors. *ACS nano*, 6(6):5635–5641, 2012.

[3] Xudong Wang, Peng Wang, Jianlu Wang, Weida Hu, Xiaohao Zhou, Nan Guo, Hai Huang, Shuo Sun, Hong Shen, Tie Lin, et al. Ultrasensitive and broadband mos2 photodetector driven by ferroelectrics. *arXiv preprint arXiv:1502.04439*, 2015.

[4] Sungjin Wi, Hyunsoo Kim, Mikai Chen, Hongsuk Nam, L Jay Guo, Edgar Meyhofer, and Xiaogan Liang. Enhancement of photovoltaic response in multilayer mos2 induced by plasma doping. *ACS nano*, 8(5):5270–5281, 2014.

[5] Cong Mai, Andrew Barrette, Yifei Yu, Yuriy G Semenov, Ki Wook Kim, Linyou Cao, and Kenan Gundogdu. Many-body effects in valleytronics: direct measurement of valley lifetimes in single-layer mos2. *Nano letters*, 14(1):202–206, 2013.

[6] Qing Hua Wang, Kourosh Kalantar-Zadeh, Andras Kis, Jonathan N Coleman, and Michael S Strano. Electronics and optoelectronics of two-dimensional transition metal dichalcogenides. *Nature nanotechnology*, 7(11):699, 2012.

[7] Haiyan Nan, Zilu Wang, Wenhui Wang, Zheng Liang, Yan Lu, Qian Chen, Daowei He, Pingheng Tan, Feng Miao, Xinran Wang, et al. Strong photoluminescence enhancement of mos2 through defect engineering and oxygen bonding. *ACS nano*, 8(6):5738–5745, 2014.

[8] Gonglan Ye, Yongji Gong, Junhao Lin, Bo Li, Yongmin He, Sokrates T Pantelides, Wu Zhou, Robert Vajtai, and Pulickel M Ajayan. Defects engineered monolayer mos2 for improved hydrogen evolution reaction. *Nano letters*, 16(2):1097–1103, 2016.

[9] Hannu Pekka Komsa, Jani Kotakoski, Simon Kurasch, Ossi Lehtinen, Ute Kaiser, and Arkady V. Krasheninnikov. Two-dimensional transition metal dichalcogenides under electron irradiation: Defect production and doping. *Physical Review Letters*, 109(3):1–5, 2012.

[10] KC Santosh, Roberto C Longo, Rafik Addou, Robert M Wallace, and Kyeongjae Cho. Impact of intrinsic atomic defects on the electronic structure of mos2 monolayers. *Nanotechnology*, 25(37):375703, 2014.

[11] TS Sreeprasad, Phong Nguyen, Namhoon Kim, and Vikas Berry. Controlled, defect-guided, metal-nanoparticle incorporation onto mos2 via chemical and microwave routes: electrical, thermal, and structural properties. *Nano letters*, 13(9):4434–4441, 2013.

[12] Hans Tornatzky, Roland Gillen, Hiroshi Uchiyama, and Janina Maultzsch. Phonon dispersion in mos_2. *Phys. Rev. B*, 99:144309, Apr 2019.

[13] William M. Parkin, Adrian Balan, Liangbo Liang, Paul Masih Das, Michael Lamparski, Carl H. Naylor, Julio A. Rodríguez-Manzo, A. T. Charlie Johnson, Vincent Meunier, and Marija Drndic. Raman shifts in electron-irradiated monolayer mos2. *ACS Nano*, 10(4):4134–4142, 2016. PMID: 26998814.

[14] Soungmin Bae, Natsuki Sugiyama, Takatoshi Matsuo, Hannes Raebiger, Ken-ichi Shudo, and Koichi Ohno. Defect-induced vibration modes of ar^+-irradiated mos_2. *Phys. Rev. Applied*, 7:024001, Feb 2017.

[15] Arsalan Hashemi, Arkady V. Krasheninnikov, Martti Puska, and Hannu-Pekka Komsa. Efficient method for calculating raman spectra of solids with impurities and alloys and its application to two-dimensional transition metal dichalcogenides. *Phys. Rev. Materials*, 3:023806, Feb 2019.

[16] Manijeh Razeghi. *Fundamentals of solid state engineering*. Springer, 2006.

[17] Martin T Dove and Martin T Dove. *Introduction to lattice dynamics*, volume 4. Cambridge university press, 1993.

[18] Formulations — Phonopy v.2.0.0.

[19] Peter Y. Yu and Manuel Cardona. *Fundamentals of semiconductors : physics and materials properties*. Springer, 2010.

[20] Ye-Cheng Zhou, Hao-Li Zhang, and Wei-Qiao Deng. A 3nrule for the electronic properties of doped graphene. *Nanotechnology*, 24(22):225705, may 2013.

[21] Fawei Zheng and Ping Zhang. Phonon dispersion unfolding in the presence of heavy breaking of spatial translational symmetry. *Computational Materials Science*, 125, 02 2016.

[22] Stefano Baroni, Stefano de Gironcoli, and Paolo Giannozzi. Phonon dispersions in ga_x $al_{1-x}as$ alloys. *Phys. Rev. Lett.*, 65:84–87, Jul 1990.

[23] Xin Zhang, Xiao-Fen Qiao, Wei Shi, Jiang-Bin Wu, De-Sheng Jiang, and Ping-Heng Tan. Phonon and raman scattering of two-dimensional transition metal dichalcogenides from monolayer, multilayer to bulk material. *Chemical Society Reviews*, 44(9):2757–2785, 2015.

[24] M Kan, JY Wang, XW Li, SH Zhang, YW Li, Y Kawazoe, Q Sun, and P Jena. Structures and phase transition of a mos2 monolayer. *The Journal of Physical Chemistry C*, 118(3):1515–1522, 2014.

[25] Keenan E Dungey, M David Curtis, and James E Penner-Hahn. Structural characterization and thermal stability of mos2 intercalation compounds. *Chemistry of Materials*, 10(8):2152–2161, 1998.

[26] Valentin Alexiev, Roel Prins, and Thomas Weber. Ab initio study of mos 2 and li adsorbed on the (101 [combining macron] 0) face of mos 2. *Physical Chemistry Chemical Physics*, 2(8):1815–1827, 2000.

[27] Alexander V Kolobov and Junji Tominaga. *Two-Dimensional Transition-Metal Dichalcogenides*, volume 239. Springer, 2016.

[28] Zhong Lin, Bruno R Carvalho, Ethan Kahn, Ruitao Lv, Rahul Rao, Humberto Terrones, Marcos A Pimenta, and Mauricio Terrones. Defect engineering of two-dimensional transition metal dichalcogenides. *2D Materials*, 3(2):022002, 2016.

[29] Ashok Kumar and PK Ahluwalia. A first principle comparative study of electronic and optical properties of 1h–mos2 and 2h–mos2. *Materials Chemistry and Physics*, 135(2-3):755–761, 2012.

[30] A. Kumar and P. K. Ahluwalia. Electronic structure of transition metal dichalcogenides monolayers 1h-mx2 (m = mo, w; x = s, se, te) from ab-initio theory: new direct band gap semiconductors. *The European Physical Journal B*, 85(6):186, Jun 2012.

[31] Eugene S Kadantsev and Pawel Hawrylak. Electronic structure of a single mos2 monolayer. *Solid State Communications*, 152(10):909–913, 2012.

[32] HSS Ramakrishna Matte, A Gomathi, Arun K Manna, Dattatray J Late, Ranjan Datta, Swapan K Pati, and CNR Rao. Mos2 and ws2 analogues of graphene. *Angewandte Chemie International Edition*, 49(24):4059–4062, 2010.

[33] Mildred S Dresselhaus, Gene Dresselhaus, and Ado Jorio. Applications of group theory to the physics of solids, 2008.

[34] Jinhua Hong, Zhixin Hu, Matt Probert, Kun Li, Danhui Lv, Xinan Yang, Lin Gu, Nannan Mao, Qingliang Feng, Liming Xie, et al. Exploring atomic defects in molybdenum disulphide monolayers. *Nature communications*, 6:6293, 2015.

[35] D. Liu, Y. Guo, L. Fang, and J. Robertson. Sulfur vacancies in monolayer mos2 and its electrical contacts. *Applied Physics Letters*, 103(18):183113, 2013.

[36] Hannu-Pekka Komsa and Arkady V. Krasheninnikov. Native defects in bulk and monolayer mos_2 from first principles. *Phys. Rev. B*, 91:125304, Mar 2015.

[37] Mahdi Ghorbani-Asl, Silvan Kretschmer, Douglas E Spearot, and Arkady V Krasheninnikov. Two-dimensional MoS2 under ion irradiation: from controlled defect production to electronic structure engineering. *2D Materials*, 4(2):025078, apr 2017.

[38] Donald W Brenner, Olga A Shenderova, Judith A Harrison, Steven J Stuart, Boris Ni, and Susan B Sinnott. A second-generation reactive empirical bond order (rebo) potential energy expression for hydrocarbons. *Journal of Physics: Condensed Matter*, 14(4):783, 2002.

[39] John Edward Jones. On the determination of molecular fields.—ii. from the equation of state of a gas. *Proceedings of the Royal Society of London. Series A, Containing Papers of a Mathematical and Physical Character*, 106(738):463–477, 1924.

[40] Steven J Plimpton and Aidan P Thompson. Computational aspects of many-body potentials. *MRS bulletin*, 37(5):513–521, 2012.

[41] J. Tersoff. New empirical approach for the structure and energy of covalent systems. *Phys. Rev. B*, 37:6991–7000, Apr 1988.

[42] J Tersoff. Modeling solid-state chemistry: Interatomic potentials for multicomponent systems. *Physical Review B*, 39(8):5566, 1989.

[43] G. Kresse and J. Hafner. Ab initio molecular dynamics for liquid metals. *Phys. Rev. B*, 47:558–561, Jan 1993.

[44] John P. Perdew, Kieron Burke, and Matthias Ernzerhof. Generalized gradient approximation made simple. *Phys. Rev. Lett.*, 77:3865–3868, Oct 1996.

[45] Dirk Porezag and Mark R. Pederson. Infrared intensities and raman-scattering activities within density-functional theory. *Phys. Rev. B*, 54:7830–7836, Sep 1996.

[46] A Togo and I Tanaka. First principles phonon calculations in materials science. *Scr. Mater.*, 108:1–5, Nov 2015.

[47] Sandro Mignuzzi, Andrew J. Pollard, Nicola Bonini, Barry Brennan, Ian S. Gilmore, Marcos A. Pimenta, David Richards, and Debdulal Roy. Effect of disorder on raman scattering of single-layer Mos_2. *Phys. Rev. B*, 91:195411, May 2015.

[48] C. Rice, R. J. Young, R. Zan, U. Bangert, D. Wolverson, T. Georgiou, R. Jalil, and K. S. Novoselov. Raman-scattering measurements and first-principles calculations of strain-induced phonon shifts in monolayer mos_2. *Phys. Rev. B*, 87:081307, Feb 2013.

Appendix A

Scripts for building defective samples

In this chapter I attached the MATLAB script only for making MoS2 antisite sample. The scripts for other point defects are simpler than this one.

The main part is:

```
clear all;
clc;

%below three lines are the POSCAR file, in which the atom_number.dat ...
    provide the information of the number of Mo and S atoms, ...
    atom_position.dat is the atom position (3*n matrix), and the ...
    cell_size.dat is the 3*3 lattice parameter matrix.
load atom_number.dat;
load atom_position.dat;
load cell_size.dat;

for i=1:5
    for Percent=5:5
        percent=round(Percent*atom_number(1)*0.01);
        [atom_number_after,atom_position_after,moved_atoms]=
        make_mos2_defect(atom_number,atom_position,percent);

        dirtory=['00',num2str(i),'/','contration',num2str(Percent)];
        geo=[dirtory,'/geo'];
        mkdir(dirtory);
        mkdir(geo);
        D=[geo,'/POSCAR'];
        fid=fopen(D,'wt');
        fprintf(fid,'MoS2\n');
        fprintf(fid,' %2.1f\n',1.0);
        format long eng;
        fprintf(fid,'  %16.14f  %16.14f  %16.14f\n',cell_size');
        fprintf(fid,'  Mo   S\n');
        fprintf(fid,'    %d   ...
           %d\n',atom_number_after(1),atom_number_after(2));
        fprintf(fid,'Cartesian\n');
        fprintf(fid,' %16.14f  %16.14f  %16.14f\n',atom_position_after');
        fclose(fid);

        Beifen=[geo,'/001Beifen'];
```

```
        fid=fopen(Beifen,'wt');
        fprintf(fid,'MoS2\n');
        fprintf(fid,' %2.1f\n',1.0);
        format long eng;
        fprintf(fid,'  %16.14f  %16.14f  %16.14f\n',cell_size');
        fprintf(fid,'  Mo   S   S\n');
        fprintf(fid,'    %d   %d   %d\n',100,100,100);

        Beifen2=[geo,'/002Beifen'];
        fid=fopen(Beifen2,'wt');
        fprintf(fid,' %16.14f  %16.14f  %16.14f\n',moved_atoms');
    end
end
```

The make_mos2_defect.m file:

```
function [atom_number_after,atom_position_after,moved_atoms] = ...
    make_mos2_defect(atom_number,atom_position,percent)

Mo    = atom_position(1:atom_number(1),:);
S_top = atom_position(atom_number(1)+1:atom_number(2),:);
S_bot = atom_position(atom_number(2)+1:atom_number(1)+atom_number(2),:);
moved_atom_top=zeros(percent,3);
moved_atom_bot=zeros(percent,3);



for i=1:percent
    Defectable=length(S_top);
    Rand=randi(Defectable);
    Mo_insert=[S_top(Rand,1:2),Mo(1,3)];
    moved_atom_top(i,:)=S_top(Rand,:);
    moved_atom_bot(i,:)=S_bot(Rand,:);
    S_top(Rand,:)=[];
    S_bot(Rand,:)=[];
    Mo=[Mo;Mo_insert];
end

atom_number_after=[length(Mo),length(S_top)*2];
atom_position_after=[Mo;S_top;S_bot];
moved_atoms=[moved_atom_top;moved_atom_bot];


end
```

Appendix B

Script for calculating RGDOS

Use python 2.6 to run all the Python scripts in this thesis.

```
import re
import csv
from decimal import *
import numpy as np
import matplotlib.pyplot as plt
from sys import exit, argv
from math import copysign

POSCAR_pc = argv[1]
POSCAR_sc = argv[2]
VIBMOD_pc = argv[3]
VIBMOD_sc = argv[4]
Ramannode = int(argv[5])

#Here we calculate the E'' and A''2 mode
if Ramannode == 8:
    coeff = 0.5
elif Ramannode == 6:
    coeff = 1.0
else:
    coeff = 0

def Gaussian(x, miu, sigma):
    Y = np.exp((x-miu)**2/(-2*sigma**2))
    return Y

def nun_atom(poscar):
    lines = poscar.readlines()
    poscar.seek(0)

    scale = float(lines[1])
    if scale < 0.0:
        print("Negative scale is not correct in %s!" %poscar)
        exit(1)

    try:
        atoms = [int(x) for x in lines[5].split()]
    except ValueError:
```

```
39          atoms = [int(x) for x in lines[6].split()]
40      return atoms
41
42  def vol(poscar):
43      lines = poscar.readlines()
44      poscar.seek(0)
45
46      scale = float(lines[1])
47      if scale < 0.0:
48          print("Negative scale is not correct in %s" %poscar)
49
50      lat_vec = []
51      for i in range(2,5):
52          lat_vec.append([float(x)*scale for x in lines[i].split()[:3]])
53
54
55      vol = np.linalg.det(lat_vec)
56      return vol, lat_vec
57
58  def read_modes(qpointsyaml):
59      lines = qpointsyaml.xreadlines()
60
61      if int(lines.next().split()[-1]) !=1:
62          print("To calculate RGDOS you need only QPOINTS = 0.0 0.0 0.0")
63          exit(1)
64
65      number_of_atoms = int(lines.next().split()[-1])
66      number_of_modes = 3 * number_of_atoms
67      frequencies = np.zeros(number_of_modes)
68      polarization_vectors = np.zeros((number_of_modes,number_of_atoms,3))
69
70      i = -1
71      for line in lines:
72          if "frequency" in line:
73              j = -1
74              i += 1
75              frequencies[i] = float(line.split()[-1])
76          if "    - # atom " in line:
77              j += 1
78              for k in range(3):
79                  polarization_vectors[i,j,k] = ...
                        float(lines.next().split()[2].replace(',',''))
80      return number_of_atoms, number_of_modes, ...
            polarization_vectors,frequencies
81
82  with open(POSCAR_pc,"r") as pc, open(POSCAR_sc,"r") as sc:
83
84      SC_VOL, SC_LAT = vol(sc)
85      PC_VOL, PC_LAT = vol(pc)
86      natsc = nun_atom(sc)
87      natpc = nun_atom(pc)
88      vol_sc_topc = SC_VOL/PC_VOL
89
90      if abs(vol_sc_topc - round(vol_sc_topc)) > 0.0001 or vol_sc_topc ...
            < 1:
91          print("Supercell is not cosistent with primitive cell\
```

```
92                 OR the oreder of argv is not correct.")
93         exit(1)
94
95 with open(VIBMOD_pc,'r') as vibpc, open(VIBMOD_sc,'r') as vibsc:
96
97     natoms_sc, nmodes_sc, vibmodes_sc, frequencies_sc = read_modes(vibsc)
98     natoms_pc, nmodes_pc, vibmodes_pc, frequencies_pc = read_modes(vibpc)
99
100    ucR = int(Ramannode) - 1
101    pristine_vibs = np.zeros((natoms_sc, 3))
102
103    weight = np.zeros((nmodes_sc))
104
105    for uatm in range(len(natsc)):
106        if uatm == 0:
107            a = 0
108            b = natsc[uatm]
109        else:
110            a = sum(natsc[:uatm])
111            b = sum(natsc[:uatm+1])
112
113        for j in range(a,b):
114            for k in range(3):
115                pristine_vibs[j, k] = vibmodes_pc[ucR, uatm, k]
116
117    for scm in range(0,nmodes_sc):
118        for scat in range(natoms_sc):
119            weight[scm] += np.dot(vibmodes_sc[scm, scat], ...
                pristine_vibs[scat])
120
121 num = 5000
122 FREQUENCY = np.linspace(0,16.498858519,num)
123 INTENSITY = np.zeros((num))
124
125 for i in range(nmodes_sc):
126     for k in range(num):
127         INTENSITY[k] += abs(weight[i]) * Gaussian(FREQUENCY[k], ...
            frequencies_sc[i], 0.05)
128
129 maxi = 1
130
131 with open("RGDOS_%s.dat"%Ramannode,"w") as f:
132     writer = csv.writer(f, delimiter='\t')
133     writer.writerows(zip(33.335639515*FREQUENCY, coeff*(INTENSITY/maxi)))
```

Appendix C

Scripts for phonon unfolding

This script is for calculating the qpoints for SC. It needs the qpoints for PC and the POSCAR files of PC and SC. Note that the calculated qpoints are not only in the FBZ, because it is easier to match the qpoints of PC.

```
import re
import csv
from decimal import *
import numpy as np
import matplotlib.pyplot as plt
from sys import exit, argv
from math import copysign

POSCAR_pc = argv[1]
POSCAR_sc = argv[2]
VIBMOD_pc = argv[3]

def vol(poscar):
    lines = poscar.readlines()
    poscar.seek(0)

    scale = float(lines[1])
    if scale < 0.0:
        print("Negative scale is not correct in %s" %poscar)
    lat_vec = []
    for i in range(2,5):
        lat_vec.append([float(x)*scale for x in lines[i].split()[:3]])
    vol = np.linalg.det(lat_vec)
    lat_vec=np.array(lat_vec)
    return vol, lat_vec

def read_modes(qpointsyaml):
    lines = qpointsyaml.xreadlines()
    number_of_qpoints= int(lines.next().split()[-1])
    qpoints         = np.zeros((number_of_qpoints,3))
    Q = -1
    for line in lines:
        if "q-position" in line:
            Q += 1
            qpoints[Q] = re.findall(r"\d+\.?\d*",line)
```

```
36          qpoints=np.array(qpoints)
37      return number_of_qpoints, qpoints
38
39  with open(POSCAR_pc,"r") as pc, open(POSCAR_sc,"r") as sc:
40      SC_VOL, SC_LAT = vol(sc)
41      PC_VOL, PC_LAT = vol(pc)
42
43      vol_sc_topc = SC_VOL/PC_VOL
44
45      if abs(vol_sc_topc - round(vol_sc_topc)) > 0.0001 or vol_sc_topc ...
           < 1:
46          print("Supercell is not cosistent with primitive cell\OR the ...
               oreder of argv is not correct.")
47          exit(1)
48  ############################## here I need to add the angle of the ...
       k_vector so that it can
49  ############################calculate all materials.
50      k_a_pc = 1/PC_LAT[0,0]
51      k_b_pc = 1/np.linalg.norm([PC_LAT[1,0],PC_LAT[1,1]])
52      k_a_sc = 1/SC_LAT[0,0]
53      k_b_sc = 1/np.linalg.norm([SC_LAT[1,0],SC_LAT[1,1]])
54
55      a_time=k_a_pc/k_a_sc
56      b_time=k_b_pc/k_b_sc
57
58      k_vec_pc=np.array([a_time,b_time,0])
59
60      print(k_vec_pc)
61      k_vec_sc=np.array([1,1,0])
62
63  with open(VIBMOD_pc,'r') as vibpc:
64      nqpoints_pc, qpoints_pc = read_modes(vibpc)
65      qpoint_pc=np.zeros((nqpoints_pc,3))
66
67      qposition_pc=qpoints_pc*k_vec_pc
68
69      qposition_sc=qposition_pc
70      qposition_sc=np.array(qposition_sc)
71      print(qposition_sc)
72
73  f=open("QPOINTS","wt")
74  f.write('%d\n' %nqpoints_pc)
75  np.savetxt(f,qposition_sc,fmt="%.4f")
76  f.close()
```

This script is the main script to calculate the unfolded phonon dispersions for SC.

```
1  import re
2  import csv
3  from decimal import *
4  import numpy as np
5  import matplotlib.pyplot as plt
6  from sys import exit, argv
7  from math import copysign
8
```

```
#this script needs qpoints.yaml from Phonopy calculation. Both PC and ...
    SC are needed.

POSCAR_pc = argv[1]
POSCAR_sc = argv[2]
VIBMOD_pc = argv[3]
VIBMOD_sc = argv[4]

def get_number(x):
    return re.findall(r"[-+]?\d*\.\d+|\d+",x)

def getMax( M ):
    maxVal = 0
    for row in M:
        if max(row) > maxVal:
            maxVal = max(row)
    return maxVal

def nun_atom(poscar):
    lines = poscar.readlines()
    poscar.seek(0)

    scale = float(lines[1])
    if scale < 0.0:
        print("Negative scale is not correct in %s!" %poscar)
        exit(1)

    try:
        atoms = [int(x) for x in lines[5].split()]
    except ValueError:
        atoms = [int(x) for x in lines[6].split()]
    return atoms

def vol(poscar):
    lines = poscar.readlines()
    poscar.seek(0)

    scale = float(lines[1])
    if scale < 0.0:
        print("Negative scale is not correct in %s" %poscar)

    lat_vec = []
    for i in range(2,5):
        lat_vec.append([float(x)*scale for x in lines[i].split()[:3]])

    vol = np.linalg.det(lat_vec)
    return vol, lat_vec

def read_modes(qpointsyaml):
    lines = qpointsyaml.xreadlines()
    number_of_qpoints= int(lines.next().split()[-1])
    qpoints          = np.zeros((number_of_qpoints,3))
    number_of_atoms = int(lines.next().split()[-1])
    number_of_modes = 3 * number_of_atoms
    frequencies = np.zeros((number_of_qpoints,number_of_modes))
    polarization_vectors = ...
```

```
        np.zeros((number_of_qpoints,number_of_modes,number_of_atoms,3,2)) ...
        #the 2 here is the real and imagry part of the x,y,z ...
        direction vibrations.
    Q = -1
    for line in lines:
        if "q-position" in line:
            i = -1
            Q += 1
            qpoints[Q] = re.findall(r"\d+\.?\d*",line)
        if "frequency" in line:
            j = -1
            i += 1
            frequencies[Q,i] = float(line.split()[-1])
        if "    - # atom " in line:
            j += 1
            for k in range(3):
                polarization_vectors[Q,i,j,k] = get_number(lines.next())
    qpoints=np.array(qpoints)
    return number_of_qpoints, number_of_atoms, number_of_modes, ...
        polarization_vectors, qpoints, frequencies

with open(POSCAR_pc,"r") as pc, open(POSCAR_sc,"r") as sc:
    SC_VOL, SC_LAT = vol(sc)
    PC_VOL, PC_LAT = vol(pc)
    natsc = nun_atom(sc)  #I only care this
    natpc = nun_atom(pc)
    vol_sc_topc = SC_VOL/PC_VOL

with open(VIBMOD_pc,'r') as vibpc, open(VIBMOD_sc,'r') as vibsc:
    nqpoints_sc, natoms_sc, nmodes_sc, vibmodes_sc, qpoints_sc, ...
        frequencies_sc = read_modes(vibsc)
    nqpoints_pc, natoms_pc, nmodes_pc, vibmodes_pc, qpoints_pc, ...
        frequencies_pc = read_modes(vibpc)

    weight=np.zeros((nqpoints_pc,nmodes_sc)) #unfold, the qpoints ...
        should be the same as PC.
    weight_middle=np.zeros((nmodes_pc,nqpoints_pc,nmodes_sc)) ...
        #tperpare for normalization of each pristine mode.
    pristine_vibs=np.zeros((nqpoints_pc,nmodes_pc,sum(natsc),3,2))

    ################################this part is to match the atom in ...
        PC and SC, only works for atoms in PC is easy to devide.
    for uatm in range(len(natsc)):
        if uatm == 0:
            a = 0
            b = natsc[uatm]
        else:
            a = sum(natsc[:uatm])
            b = sum(natsc[:uatm+1])


        for Q in range(nqpoints_pc):
            for i in range(nmodes_pc):
                for j in range(a,b):
                    for k in range(3):
                            pristine_vibs[Q, i, j, k] = ...
```

```
                                    vibmodes_pc[Q, i, uatm, k]
    ###############################################################

    for Qpc in range(nqpoints_pc):
        for Msc in range(nmodes_sc):
            for Mpc in range(nmodes_pc):
                #for Qsc in range(nqpoints_sc):
                    for Asc in range(natoms_sc):
                        for k in range(3):
                            weight_middle[Mpc,Qpc,Msc] += ...
                                np.dot(vibmodes_sc[Qpc,Msc,Asc,k],
                            pristine_vibs[Qpc,Mpc,Asc,k])
        print(Qpc,Msc)

    ##########################
weight_middle=np.array(weight_middle)
weight_middle=weight_middle**2
for i in range(nmodes_pc):
    for j in range(nqpoints_pc):
        max_weight=max(weight_middle[i,j])
        weight_middle[i,j] =weight_middle[i,j]/max_weight

for i in range(nmodes_pc):
    for j in range(nqpoints_pc):
        for k in range(nmodes_sc):
            weight[j,k]+=weight_middle[i,j,k]

for j in range(nqpoints_pc):
    for k in range(nmodes_sc):
        if weight[j,k]>1:
            weight[j,k]=1

frequencies_sc=np.array(frequencies_sc)
qpoints_pc=np.array(qpoints_pc)
final=np.zeros((nqpoints_pc,nmodes_sc,3))
frequency=33.335639515*frequencies_sc

np.savetxt("weight",weight,fmt="%.4f")
np.savetxt("frequency",frequency,fmt="%.6f")
np.savetxt("qpoints-sc",qpoints_sc,fmt="%.4f")

print(nqpoints_pc,nmodes_sc)


mpl_fig = plt.figure()
ax = mpl_fig.add_subplot(111)
x_ticks=[0,172,272,472]
for i in range(nqpoints_pc):
    for j in range(nmodes_sc):
        if weight[i,j]>0.05:
            plt.plot(i,frequency[i,j],marker='.',
            markersize=2*weight[i,j]+3,color=((1,0,0,weight[i,j])))
plt.xlim((0, nqpoints_pc))
plt.ylim((0, 520))
ax.set_ylabel("Frequency (1/cm)",fontsize=18)
plt.xticks(x_ticks)
```

```
165 plt.savefig('unfold.png')
166 plt.show()
```

Appendix D

Script for localize vibrations

```
import re
import csv
from decimal import *
import numpy as np
import matplotlib.pyplot as plt
from sys import exit, argv
from math import copysign
import pandas as pd

POSCAR_pc = argv[1]
POSCAR_sc = argv[2]
VIBMOD_pc = argv[3]
VIBMOD_sc = argv[4]
Ramannode = argv[5]

sigma = 0.05;

def Gaussian(x, miu, sigma):
    Y = np.exp((x-miu)**2/(-2*sigma**2))
    return Y

def get_number(x):
    return re.findall(r"[-+]?\d*\.\d+|\d+",x)

def index(filename, words):
        for line_number, line in enumerate(filename, 1):
            word = line.strip()
            if word in words:
                return line_number

#####################################################################
def nun_atom(poscar):
    lines = poscar.readlines()
    poscar.seek(0)

    scale = float(lines[1])
    if scale < 0.0:
        print("Negative scale is not correct in %s!" %poscar)
        exit(1)
```

```
40
41      try:
42          atoms = [int(x) for x in lines[5].split()]
43      except ValueError:
44          atoms = [int(x) for x in lines[6].split()]
45      return atoms
46
47  def vol(poscar):
48      lines = poscar.readlines()
49      poscar.seek(0)
50
51      scale = float(lines[1])
52      if scale < 0.0:
53          print("Negative scale is not correct in %s" %poscar)
54
55      lat_vec = []
56      for i in range(2,5):
57          lat_vec.append([float(x)*scale for x in lines[i].split()[:3]])
58
59
60      vol = np.linalg.det(lat_vec)
61      return vol, lat_vec
62
63  def read_modes(qpointsyaml):
64      lines = qpointsyaml.xreadlines()
65
66      if int(lines.next().split()[-1]) !=1:
67          print("To calculate RGDOS you need only QPOINTS = 0.0 0.0 0.0")
68          exit(1)
69
70      number_of_atoms = int(lines.next().split()[-1])
71      number_of_modes = 3 * number_of_atoms
72      frequencies = np.zeros(number_of_modes)
73      polarization_vectors = np.zeros((number_of_modes,number_of_atoms,3))
74
75      i = -1
76      for line in lines:
77          if "frequency" in line:
78              j = -1
79              i += 1
80              frequencies[i] = float(line.split()[-1])
81          if "    - # atom " in line:
82              j += 1
83              for k in range(3):
84                  polarization_vectors[i,j,k] = ...
                        float(lines.next().split()[2].replace(',',''))
85      return number_of_atoms, number_of_modes, ...
            polarization_vectors,frequencies
86
87  with open(POSCAR_pc,"r") as pc, open(POSCAR_sc,"r") as sc:
88
89      SC_VOL, SC_LAT = vol(sc)
90      PC_VOL, PC_LAT = vol(pc)
91      natsc = nun_atom(sc)
92      natpc = nun_atom(pc)
93      vol_sc_topc = SC_VOL/PC_VOL
```

```
94
95 with open(VIBMOD_pc,'r') as vibpc, open(VIBMOD_sc,'r') as vibsc:
96
97     natoms_sc, nmodes_sc, vibmodes_sc, frequencies_sc = read_modes(vibsc)
98     natoms_pc, nmodes_pc, vibmodes_pc, frequencies_pc = read_modes(vibpc)
99
100    ucR = int(Ramannode) - 1
101    pristine_vibs = np.zeros((natoms_sc, 3))
102
103    weight = np.zeros((nmodes_sc))
104
105    for uatm in range(len(natsc)):
106        if uatm == 0:
107            a = 0
108            b = natsc[uatm]
109        else:
110            a = sum(natsc[:uatm])
111            b = sum(natsc[:uatm+1])
112
113        for j in range(a,b):
114            for k in range(3):
115                pristine_vibs[j, k] = vibmodes_pc[ucR, uatm, k]
116
117    for scm in range(3,nmodes_sc):
118        for scat in range(natoms_sc):
119            weight[scm] += np.dot(vibmodes_sc[scm, scat], ...
                pristine_vibs[scat])
120
121
122 weight=abs(weight)
123 maxi = max(weight)
124 WEIGHT=weight/maxi
125
126 #### Find Gausian peak
127
128 num = 3000
129 FREQUENCY_gaussain = ...
    np.linspace(min(frequencies_sc),2+max(frequencies_sc),num)
130 INTENSITY = np.zeros((num))
131
132 for i in range(nmodes_sc):
133     for k in range(num):
134         INTENSITY[k] += weight[i] * Gaussian(FREQUENCY_gaussain[k], ...
            frequencies_sc[i], sigma)
135 maxi_gaussain = max(INTENSITY )
136
137 #### calculate each modes' weight on the peak
138
139 peak_weight  = np.zeros((nmodes_sc))
140 peak_position  = np.argmax(INTENSITY)
141 peak_frequency = FREQUENCY_gaussain[peak_position]
142
143
144 for i in range(nmodes_sc):
145     peak_weight[i] = weight[i] * Gaussian(peak_frequency, ...
        frequencies_sc[i], sigma)/maxi_gaussain
```

```
146
147 #### write vibration modes
148
149 VIBRATION_MODES        =np.zeros((natoms_sc,1))
150 VIBRATION_MODES_combine=np.zeros((natoms_sc,1))
151 FREQUENCY = []
152 frequencies_sc2=frequencies_sc*33.335639515
153 PEAK_FREQUENCY=peak_frequency*33.335639515
154
155 for scm in range(3,nmodes_sc):
156      if frequencies_sc2[scm]>(PEAK_FREQUENCY-1.666781976) and ...
          frequencies_sc2[scm]<(PEAK_FREQUENCY+1.666781976):
157         FREQUENCY.append([int(scm+1),frequencies_sc2[scm],WEIGHT[scm]])
158         for scat in range(natoms_sc):
159             VIBRATION_MODES_combine[scat] ...
                +=WEIGHT[scm]*np.dot(vibmodes_sc[scm, ...
                scat],vibmodes_sc[scm, scat])
160
161 for scat in range(natoms_sc):
162     VIBRATION_MODES[scat]=VIBRATION_MODES_combine[scat]
163
164 ######################################################################
165
166
167 f2=open("POSCAR-sc.xsf", "r")
168 b1=f2.readlines()[11:]
169 f2.close()
170
171 for i in range(natoms_sc):
172      b1[i]=b1[i].rstrip()+'   '+str(VIBRATION_MODES[i,0])+'\n'
173
174
175 f3=open("vib_mod_dis_%s"%Ramannode, "w")
176 for line in b1:
177     f3.write(line)
178 f3.close()
179
180 FREQUENCY=np.array(FREQUENCY)
181 if FREQUENCY!=[]:
182     FREQUENCY = FREQUENCY[FREQUENCY[:,2].argsort()]
183 else:
184     FREQUENCY=np.matrix([0,0,0])
185
186 lalala=len(FREQUENCY)
187 c1=[]
188 c1.append('Mode_No.'+'   '+'Frequency'+'   '+'Weight'+'\n')
189 for i in range(lalala):
190     c1.append(str(int(FREQUENCY[i,0]))+'     '+str(FREQUENCY[i,1])+' ...
            '+str(FREQUENCY[i,2])+'\n')
191
192 f4=open("frequency_list_%s"%Ramannode, 'w')
193 for line in c1:
194     f4.write(line)
195 f4.close()
```